

HF Aurora Reflections Observed at Anchorage, Alaska USA

Part 1 ~ Concepts

Whitham D. Reeve

1-1. Introduction



While processing the data for my studies of radio blackouts and sudden frequency deviations [Reeve15-1], [Reeve15-2] and meteor trail reflections [Reeve21] in the high frequency band, I noticed many instances of unusual spectra around local solar midnight that coincided with geomagnetic disturbances. These data were from a receiver in my Anchorage Radio Observatory, which was tuned to the WWV and WWVH time-frequency stations on 15 MHz, and the SAM-III magnetometer. Because Anchorage is on the southern edge of the auroral oval at 62° north magnetic latitude, I thought that the unusual spectra may be caused by reflections from aurora. I decided to investigate further, and this article discusses the results of that investigation. This article also includes a tutorial on the concepts and causes of aurora radio reflections.

The terms *radio aurora*, *aurora radio*, *aurora scattering*, *aurora echoes*, *aurora radio reflections* and *aurora reflections* are used interchangeably. Transmissions originate at a distant transmitter, are reflected by high-electron-density regions associated with the aurora, and are detected by a receiver as a form of *bistatic radar* (figure 1-1). Detections of aurora radio at Anchorage, in particular, involve a transmitter and receiver and reflection region separated by a distance great enough to require sky wave propagation. The phenomenon described in this article should not be confused with the distinctly different radio emissions *produced* by aurora called *aurora kilometric radiation* (or emissions).

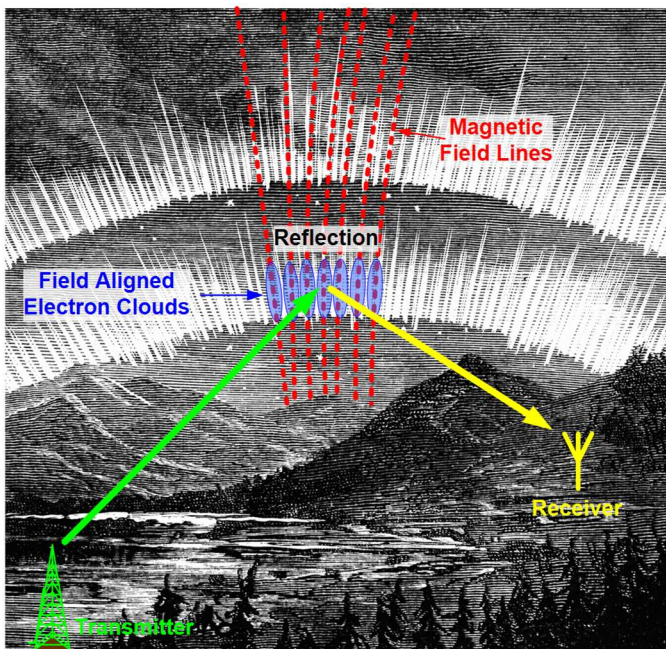


Figure 1-1 ~ Artistic representation of complex technical concepts involving aurora radio reflections. The configuration shown here, equivalent to the one discussed in this article, is a passive bistatic radar. The transmitted signal (green) is reflected by high-electron density regions associated with aurora (blue) and detected by a receiver (yellow). The signals shown here are backscattered from the distant reflection region to the receiver. The column-like reflection regions are aligned with Earth's magnetic field (red). Only a few areas of high electron density are shown but they exist all along the aurora. Although this illustration includes visible aurora, radio reflections also can occur when no aurora is visible. Underlying image source (with apologies) [Houston]

Aurora radio reflections are known to many radio amateurs who use the SAM-III magnetometer K-index Alarm feature to notify them of rapid magnetic field changes. These indicate the high probability of aurora and the possibility of *auroral communication*. The K-index is a quasi-logarithmic scale from K0 to K9 that measures the peak-to-peak magnetic flux density variations in 3-h synoptic periods. K4 or K5 often are used as the threshold for magnetic storm conditions and aurora. When the alarm annunciates, radio amateurs in the northern hemisphere point their antennas northward and attempt to communicate using the 2 m, 6 m and 10 m amateur radio bands (nominally 144, 50 and 28 MHz, respectively). Rapid amplitude and frequency fluctuations of radio aurora make voice communications very difficult, if not impossible, but CW is reported to be usable at times. On the other hand, aurora radio reflections are viewed by many radio amateurs as a form of communications interference rather than enablement.

This article follows the same basic format as {[Reeve21](#)} because many of the technical details including instrumentation are similar. For example, both meteor trail reflections and aurora radio reflections occur at approximately the same altitude and both involve columns of enhanced ionization. This article consists of two parts: **Part 1** includes a discussion of early aurora radio investigations (section 1-2), brief overview of the concepts associated with aurora radio (section 1-3), an overview of high frequency (HF) propagation (section 1-4), and the instrumentation used in the observations discussed in this article (section 1-5). A list of weblinks and references (section 1-6) and acknowledgements (section 1-7) are provided; **Part 2** consists of an overall description of the observations (section 2-1) and a selection of spectral plots, magnetograms and keograms from 2020 (section 2-2) followed by discussion (section 2-3).

1-2. Early Aurora Radio Investigations

The technical information and data in this and the next section are from the *Technical References* listed in section 1-6.

Amateur radio operators first reported aurora effects on radio propagation as far back as 1926 [QST26] with frequent reports through the 1930s and 1940s. Some early scientific investigations were funded by the US Army Signal Corps to look into the reports printed in amateur radio trade magazines and compare them to the records of visible *Northern Lights* (Aurora Borealis) observations taken at the same time. These studies confirmed the coincidence of radio aurora with visible aurora.

Extensive investigations of aurora reflections using monostatic and bistatic radars started in the early 1950s and continued through the 1960s (a monostatic radar has the receiver and transmitter collocated at a fixed location whereas a bistatic radar has the receiver and transmitter at different fixed locations). Some results of the early studies were:

- 1) Received signals had a very high fading rate roughly proportional to frequency, making voice communications mostly useless (at 50 MHz the signal fading rate was as high as 200 Hz). The high fading rate was thought to be from changes in absorption, interference between wave components, changes in the electron density or drift movement of the columnar field-aligned electron cloud,
- 2) Directional antennas gave the best results when pointed north toward the aurora (aspect sensitivity), but exceptions were observed,
- 3) No skip zones or skip effects were observed,

- 4) Polarization of the received signals changed little compared to the transmitted signals,
- 5) Although very often coincident with visible aurora, aurora radio reflections were noted when no visible aurora was present,
- 6) Radio aurora and geomagnetic activity were well correlated;
- 7) Aurora radio reflections were strongest when visible aurora had ray structure and the structure was close to the horizon,
- 8) Most aurora radio reflections occurred when visible aurora penetrated below about 110 km altitude,
- 9) Radio aurora peaked before midnight while visible aurora was most often evenly distributed about local midnight,
- 10) Strongest aurora radio reflections were received when the incident and reflected signals paths had equal angles from a line perpendicular to the magnetic field,
- 11) No aurora radio reflections were received when visible aurora was directly overhead,
- 12) Less than 1 ppm of the energy incident on the aurora was reflected back toward the receiver;
- 13) Individual radio echo features showed movements over a range of radial speeds up to approximately 1000 m s^{-1} with most below 600 m s^{-1} . In general, the sign of the velocity was positive before midnight and negative after midnight.

Almost all of the early investigations were above 30 MHz. Very little information is available on radio aurora in the HF band below 30 MHz. The main reason is that building radars at frequencies in the HF band was and still is quite difficult and, when undertaken, did not produce usable results. There is some evidence that the aurora radio reflection mechanisms may be somewhat frequency dependent (reflection at lower frequencies and reradiation, or scattering, at higher frequencies).

1-3. Aurora Radio Reflection Concepts

Visible and radio aurora are different manifestations of similar physical processes. Radio aurora, described in greater detail below, is caused by increased ionization of atoms and molecules that enables reflection of radio waves, and visible aurora is caused by atomic and molecular excitation that produces light at certain wavelengths. Radio aurora can be observed both day and night, whereas visible aurora generally cannot be seen during daylight or when clouds are present. On the other hand, in the case of the HF radio band, radio aurora may not be detectable because of unfavorable transmitter, aurora and receiver propagation path geometry or other path limitations. Radio aurora has been recorded at very low latitudes down to 25° where visible aurora is very rare.

Visible and radio aurora do share several characteristics:

- 1) Observed in the same geographic and height regions;
- 2) Correlate with geomagnetic activity;
- 3) Similar statistics of observation and motion;
- 4) Vary in a similar manner annually and over solar cycles;
- 5) Show one, two or three daily variations of peak activity (substorms).

Refer to figure 1-2 and its caption for a numbered sequence of the processes that produce visible and radio aurora, briefly summarized as follows: If the magnetic field embedded in the solar wind, called Interplanetary

Magnetic Field, or IMF, has a southward component, it may connect (merge) with Earth's northward magnetic field (this merging is much less likely if the IMF has a northward component). The open field lines associated with the connection are blown by the solar wind to the magnetotail where they reconnect. This reconnection causes plasma to flow toward Earth. The energized electrons in the plasma are trapped by the geomagnetic field lines. As the electrons approach Earth, they are energized further and precipitate into the upper atmosphere at high latitudes along magnetic field lines. The energetic particles collide with gases in the upper atmosphere producing additional ionization that is aligned with the magnetic field and dense enough to reflect radio waves. The collisions also excite the gaseous atoms and molecules producing the visible aurora.

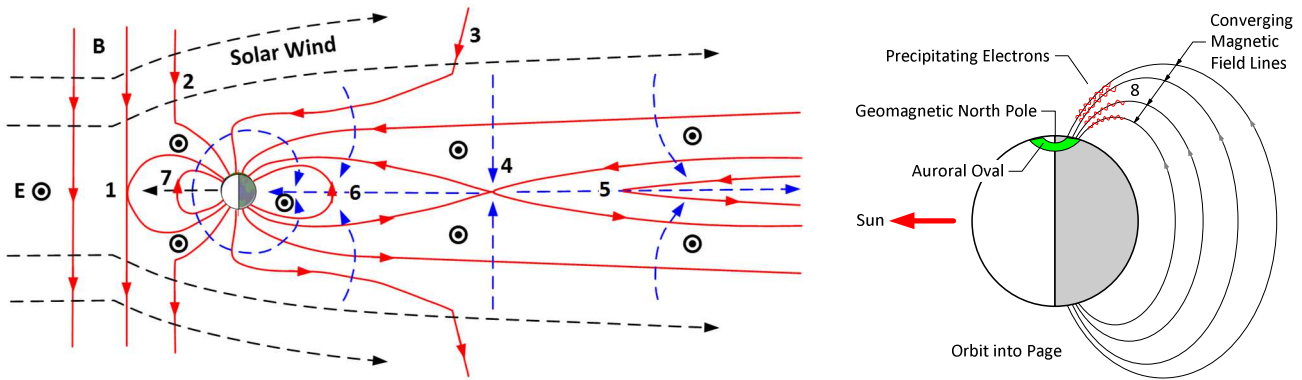


Figure 1-2 ~ Sequence of magnetic reconnection and aurora production.

Left: Cycle of magnetic reconnection called the *Dungey Cycle*. The Sun is to the left out of view, and the solar wind is flowing left-to-right shown by the gray dashed lines. The magnetic fields B are indicated by red lines and the electric fields E are indicated by small black concentric circles coming out of the page. Earth is shown as the black and white circle with the white indicating the sunlit side. Earth's magnetic field has a fixed direction northward. When the interplanetary magnetic field (IMF) embedded in the solar wind has a southward component, opposite to Earth's magnetic field, the two fields merge on the dayside of the magnetosphere in a process called magnetic reconnection ①. The formerly closed geomagnetic field lines facing the Sun open as they merge with the IMF ②. The IMF and magnetosphere are now linked and solar wind plasma can enter the magnetosphere at high latitudes. The open field lines are carried over the poles by the solar wind ③ and move to the stretched-out region on Earth's nightside called the *magnetotail*. As they stretch out, the open-field lines move toward the center plane of the tail (indicated by dashed blue lines) where they reconnect again ④, closing the magnetic flux that was opened on the dayside. The time from ① to ④ is on the order of 1 h. Part of the flux moves down-tail away from Earth ⑤ but, of interest here, part of the magnetic flux returns by internal flows to their origin. This process carries plasma resident in the magnetotail toward Earth ⑥. The highly energized electrons in the plasma are trapped by the magnetic field and further energized when they arrive within a few Earth radii by voltage variations along the magnetic field lines ⑦. The cycle may repeat in a quasi-cyclic process called a *substorm* with a period of roughly 1 to 3 h. Image adapted from: [Seki].

Right: View of Earth along the ecliptic showing electron precipitation. The energized electrons trapped by the geomagnetic field lines as explained above precipitate toward lower altitudes ⑧ where they collide with the molecules and atoms in the gaseous atmosphere. Only a few magnetic field lines on the nightside are shown but they exist all around Earth. Some of the energy transferred during collisions can substantially increase the ionization leading to reflections of radio waves from the enhanced regions. A relatively small amount of the collision energy excites the gases and produces the visible aurora. The projection of the area where visible aurora is most probable is called the *auroral oval*, colored green in this illustration, which shows only the northern auroral oval.

The streaks and curtains that are seen as the visible aurora have a base (foot) around 80 to 100 km altitude and a vertical length between 10 and 100 km. Radio aurora has a similar base but can extend to much higher altitudes. The aurora has the highest probability of occurring in an oval-shaped region centered on the geomagnetic poles called the *auroral oval* (figure 1-3).

The increased ionization at altitudes around 100 to 120 km, which corresponds to the ionosphere's E-region, is important for aurora radio reflections. At these altitudes, the increased ionization forms elongated, elliptical shaped, relatively high-density electron columns along the magnetic field lines. The higher electron densities in the columnar regions can cause radio reflections that are received on the ground if the geometry is correct for the locations of the transmitter and receiver with respect to the aurora (figure 1-4). These phenomena occur mostly on the nightside of the high-latitude regions of Earth where the aurora is most intense and most frequent, but aurora radio reflections also can occur on the dayside and at lower latitudes during geomagnetic disturbances.

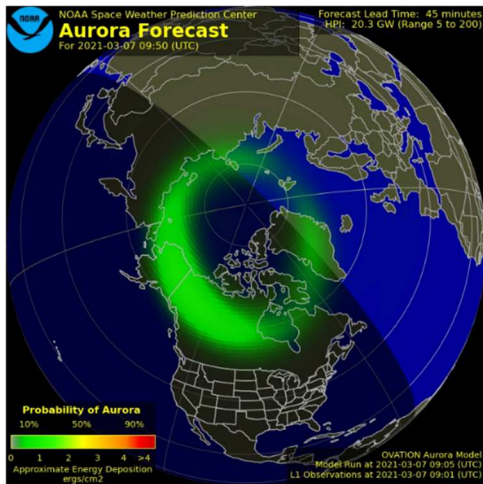


Figure 1-3 ~ Predicted northern hemisphere auroral oval for 1000 UTC on 7 March 2021 produced by the Space Weather Prediction Center. The oval, indicated by the green donut-shaped area, marks the region where aurora has a high probability of being seen overhead on a clear night. It is centered on the geomagnetic north pole and fixed with respect to the Sun, which in this image is located to the upper-right. The auroral oval rotates overhead as the Earth turns and expands and contracts with changing solar wind conditions. This image is for a slightly disturbed magnetosphere. Image source: {[SWPC-Oval](#)}.

In addition to the path propagation geometry, detecting aurora radio in the high frequency band involves ionospheric effects between the transmitter and the reflection region and between the reflection region and the receiver. The ionosphere has three characteristic frequencies that influence radio propagation: *Collision frequency*; *Gyro frequency*; and *Plasma frequency*.

Collision frequency: The collision frequency is the rate at which electrons collide with other particles. When a radio wave travels through the ionosphere, the electrons oscillate at the wave frequency. Some of the energy in the wave is lost through collisions of the electrons with neutral air atoms and molecules, thus attenuating the wave and converting kinetic energy to thermal energy.

The higher the electron collision rate with neutral air, the greater the attenuation, also called absorption. The absorption at the low end of the HF band (3 MHz) is greatest in the ionosphere's D-region because that is where the neutral air density and electron collision frequency are the highest. Absorption in both the transmit and reflected (receive) propagation paths through the ionosphere's lower region is an impediment to radio propagation. However, it should be noted that D-region absorption is primarily a daytime effect – the D-region all but disappears at night. Above the D-region, at 100 km altitudes, the collision rate is in the kilohertz range and there is little or no absorption at HF.

Gyro frequency: The gyro frequency is the rate at which electrons gyrate in a corkscrew path along magnetic field lines. The electrons are in a constant state of acceleration so they continuously emit radiation at a frequency f_g in MHz given by

$$f_g = 1 \cdot 10^{-15} (e \cdot B) / (2 \cdot \pi \cdot m_e) \quad (1)$$

where B is the magnetic flux density (nT), e is the electron charge ($1.602 \cdot 10^{-19}$ C), and m_e is the electron mass ($9.109 \cdot 10^{-31}$ kg). Since the electron charge and mass are constants, equation (1) reduces to

$$f_g = 28 \cdot 10^{-6} \cdot B \quad (2)$$

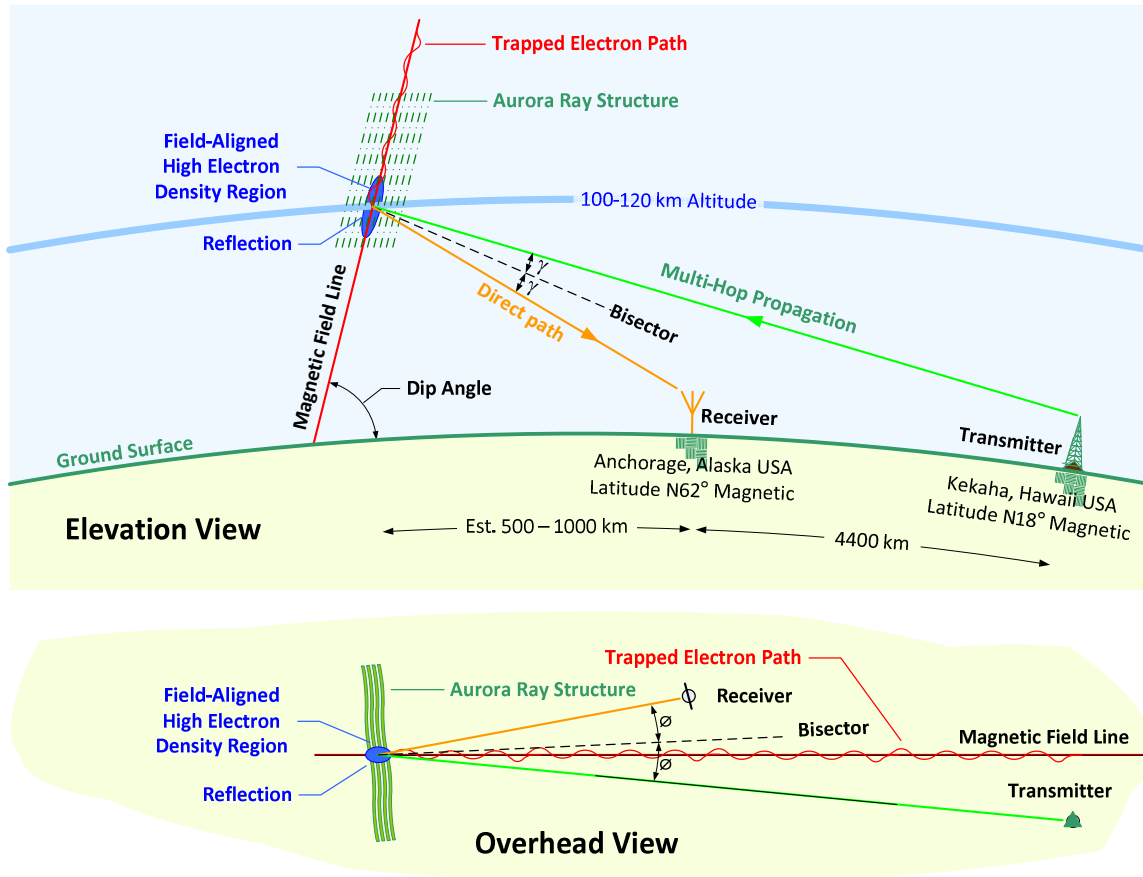


Figure 1-4 ~ Radio propagation and aurora reflection schematic. Elevation angles and scales are exaggerated for clarity; the elevation angles usually are small and reflection regions are close to the horizon as viewed from the receiver. The vertical and horizontal bisector angles, γ and ϕ , of the incident and reflected radio waves with respect to the magnetic field line are close to 90° . γ and ϕ are projections of the 3-dimensional *bistatic angle* of the propagation from the transmitter to the reflection region and back to the receiver. The transmitter and receiver locations shown in this illustration correspond to the those involved in the observations discussed in this article.

The magnetic field varies with location (latitude and longitude) and the inverse cube of the distance from Earth's center. For example, at Anchorage the magnetic flux density at the surface is approximately 55 300 nT. At 100 km altitude, the field is about 4.8% lower, or about 52 650 nT. The corresponding gyro frequencies are 1.57 and 1.50 MHz, respectively.

Plasma frequency: In the absence of a magnetic field, electrons in an ionized region – the ionosphere – have a natural resonance frequency based on their finite inertia related to their mass and an electrostatic restoring force related to their charge. This resonance frequency is called the *plasma frequency* and in MHz is given by

$$f_p = 1 \cdot 10^{-6} \left(\sqrt{N_e \cdot e^2 / \epsilon_0 \cdot m_e} \right) / 2 \cdot \pi \quad (3)$$

where N_e is the volume density of electrons (electrons m^{-3}) and ϵ_0 is the permittivity of free space ($8.854 \cdot 10^{-12}$ F m^{-1}). The electron charge e and mass m_e were given above.

An incident radio wave at a right-angle to an ionized region is reflected when its frequency is equal to or below the plasma frequency. The highest plasma frequency for reflection is called the *critical frequency*. Substituting the values for e , ϵ_0 and m in equation (3), the critical frequency in MHz is

$$f_c \approx 8.98 \cdot 10^{-6} \sqrt{N_{\max}} \quad (4)$$

For example, when the electron density N_{\max} is $2 \cdot 10^{12} m^{-3}$, the critical frequency is

$f_c \approx 8.98 \cdot 10^{-6} \cdot \sqrt{2 \cdot 10^{12}} = 12.7$ MHz. Equation (4) applies to radio waves that are perpendicular (normal) to the reflection region such as waves propagating vertically from the ground to the ionosphere or relatively low angle waves propagating to the high electron density regions in the aurora where the magnetic field lines have a large dip angle with field-aligned electron clouds. Where the radio wave is obliquely incident at an angle γ rather than perpendicular (see figure 1-4), the region can reflect much higher frequencies. The apparent critical frequency f_{ob} for oblique incidence is given by

$$f_{ob} = f_c / \cos \gamma = f_c \cdot \sec \gamma \quad (5)$$

Equation (4) can be rearranged to find the electron density that is required for reflection, as in

$$N_{\max} \approx 1.24 \cdot 10^{10} \cdot f_c^2 \quad (6)$$

For example, when the critical frequency f_c is 15 MHz, $N_{\max} = 1.24 \cdot 10^{10} \cdot (15)^2 \approx 3 \cdot 10^{12} m^{-3}$. This value is about 175 times higher than the typical nighttime electron density in the ionosphere's E-region a few hundred kilometers north of Anchorage at mid-year (figure 1-5).

Reflections at VHF and UHF require much higher electron densities than at HF [see equation (4)]. Therefore, if aurora radio reflections are received at these higher frequencies – above the apparent critical frequency – there is a possibility that the reflection mechanism involves something different, such as weak scattering (electron reradiation). This possibility is not discussed further because it is not thought to apply to the frequencies of concern here.

Radio aurora is *aspect sensitive*; that is, the radio waves are reflected most often when the angle between the geomagnetic field lines and the direction of propagation is near 90° . The observed range of off-perpendicular angles has been found to be wider at low frequencies than at high frequencies. Radio aurora usually is observed at great distances from the reflection point and *close to the horizon*.

At high latitudes, the magnetic field lines have a relatively large *dip angle*, the angle measured with respect to the horizon and also called magnetic *inclination*. For example, the dip angle at Anchorage is 74° and 1000 km north of Anchorage at the Alaska north coast is 81° . Because these angles are large, reflective geometry, in

which a relatively low elevation angle radio wave is perpendicularly incident or nearly so on the tilted columns of ionization, is highly probable. When aurora radio reflections are being received, they are from auroral columns of ionization somewhat like meteor trails having the *magnetic zenith* as the radiant.

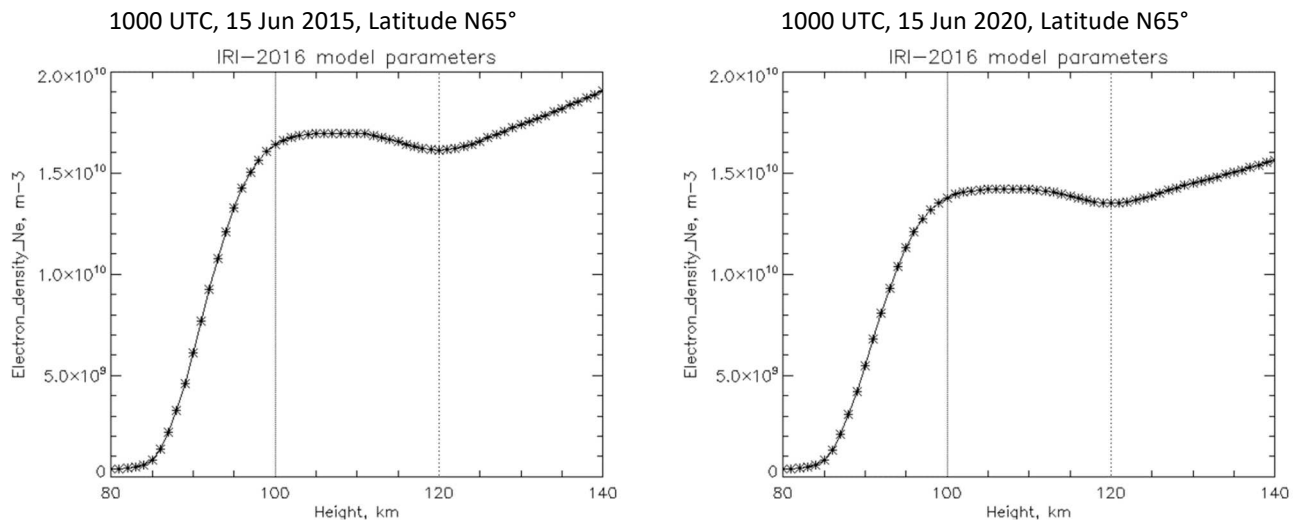


Figure 1-5 ~ Electron density profiles for altitudes of 80 to 140 km above a point about 450 km north of Anchorage during solar maximum (left) and solar minimum (right). The observations described in this article were made throughout 2020 during solar minimum. The profiles are for mid-year at 1000 UTC, which is local solar midnight. These plots were produced by the 2016 International Reference Ionosphere (IRI) model at [IRI](#).

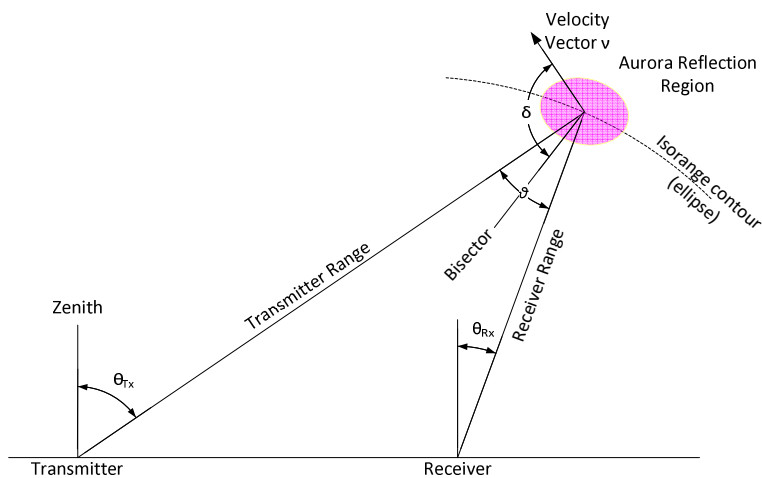


Figure 1-6 ~ Bistatic radar geometry in which the receiver and transmitter are fixed but at different locations. The reflection region (magenta ellipse) has a velocity v , which makes an angle δ with the bisector of the bistatic angle ϑ . Note that $\vartheta = \vartheta_{TX} - \vartheta_{RX}$.

The observations of aurora radio reflections involve frequency shifts of the transmitted carrier due to Doppler effects. When the transmitter and receiver are fixed, the Doppler frequency shift F_D of the received echo is given by (figure 1-6)

$$F_D = \frac{2 \cdot v}{\lambda_{TX}} \cdot \cos(\delta) \cdot \cos\left(\frac{\theta}{2}\right) = \frac{2 \cdot v \cdot f_{TX}}{c} \cdot \cos(\delta) \cdot \cos\left(\frac{\theta}{2}\right) \text{ Hz} \quad (7)$$

where λ_{TX} and f_{TX} are the transmitter carrier wavelength (m) and frequency (Hz), respectively, c is the speed of light ($m\ s^{-1}$), v is the velocity ($m\ s^{-1}$), θ is the bistatic angle (3-dimensional equivalent of 2γ and 2φ in figure 1-4) and δ is the angle between the velocity vector and bisector of the bistatic angle.

1-4. HF Propagation

Propagation concepts: For aurora radio reflections, the transmitted signals must have usable paths from the signal origination point to the aurora reflection region and from this region to the receiver. The receivers used in all of my observations were tuned to frequencies simultaneously broadcasted by the WWV transmitters near Fort Collins in Colorado and the WWVH transmitters near Kekaha on the Island of Kauai in Hawaii. The receivers are in southcentral Alaska at Anchorage, approximately 4400 km north of the WWVH transmitters and 3800 km west of the WWV transmitters (figure 1-7). Because aurora radio reflections favor north-south propagation directions, the signals of interest likely originated at WWVH. The distances are great enough to ensure that multi-hop skywave propagation is needed to reach the aurora reflection regions, estimated to be on the order of 500 to 1000 km north of Anchorage.

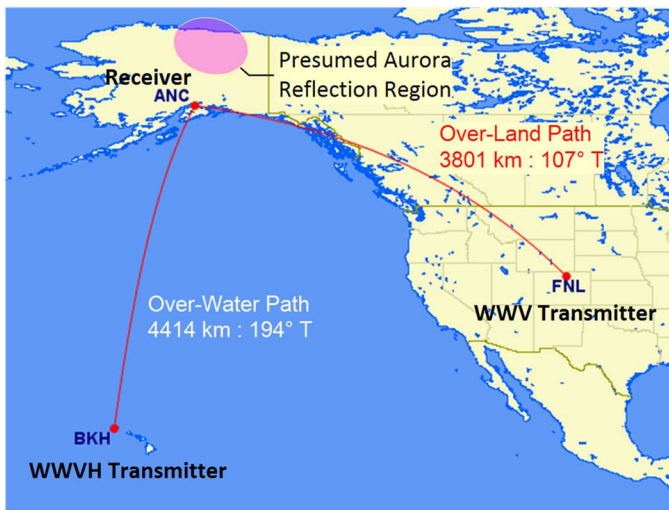


Figure 1-7 ~ Great circle paths shown in red between WWV near Fort Collins, Colorado (marked FNL) and Anchorage, Alaska (ANC) and between WWVH near Kekaha in Kauai, Hawaii (BKH) and Anchorage. As explained in the text, the likely source is WWVH. For aurora radio reflections the signals must propagate beyond Anchorage to the presumed aurora reflection region (magenta oval). The paths are long enough to require multi-hop propagation. The WWVH path is about 80% over water and encounters different propagation conditions than the WWV path, which is entirely over land. Anchorage is at the southern edge of the auroral oval, which introduces additional factors in the HF radio reflections from the aurora. Underlying image from {GCMaP}.

A system consisting of a fixed broadcast transmitter and a fixed receiver at different locations is called a *passive bistatic radar* (PBR). It is passive because the user has no control over the transmitter. The aurora reflection region is beyond the transmitter-receiver baseline, in this case north of the receiver, so the reflected signals are reflected back to Anchorage and are called backward scatter, or *backscatter* for short.

It is known that aurora radio reflections are received in the northern hemisphere most often when the transmissions are beamed northward and the reflections are received from the north. This is the case for WWVH and Anchorage. The great circle propagation path from WWVH has a reverse bearing of 194° True (178° Magnetic) at Anchorage, a near perfect south-north alignment. On the other hand, WWV is east of Anchorage on a reverse bearing of 107° True (91° Magnetic). Therefore, it is likely that aurora radio reflections received at Anchorage originated exclusively from WWVH transmitters. The discussion below will focus on that station. The WWV transmitters probably would be appropriate for receiving aurora radio reflections in Canada's Northwest Territories or Nunavut.

It is not necessary that the distances from the receiver and transmitter to the reflection region be equal but their line-of-sight distances are limited by Earth's curvature to R_{max} determined from

$$R_{max} = 2 \cdot R_E \cdot \arccos\left[\frac{R_E}{(R_E + H)}\right] \text{ km} \quad (8)$$

where R_E is Earth's radius (km, approximately 6370 km) and H is the reflection height or altitude above ground level (km). When the result of the arc-cosine calculation in equation (8) is in degrees, the factor $(\pi/180)$ radians per degree is needed to convert the arc-cosine result to radians for the remainder of the distance calculation. If the result already is in radians, the factor is not needed.

The effective Earth radius may be longer or shorter depending on the atmospheric conditions along the path. The effective Earth radius factor, K , is used to take into account these conditions. For the simple case, $K = 1$ but $K = 4/3$ often is used in propagation path analyses. In general,

$$R_{max} = 2 \cdot K \cdot R_E \cdot \arccos\left[\frac{K \cdot R_E}{(K \cdot R_E + H)}\right] \text{ km} \quad (9)$$

For the case where the aurora radio reflection height is 100 km and $K = 1$, the maximum distance calculated from equation (8) is 2240 km, or 1120 km for each half of the hop. For multi-hop HF propagation paths, equation (8) or (9) is used for individual hops and not on the entire path. For example, say propagation involves 2 hops with a total great circle distance of 4000 km. Assuming equal distances between ionospheric refraction and ground reflection points, each hop would be 2000 km and below the 2240 km maximum.

To explain aurora radio reflections from transmitters on the order of 4000 km away from the receiver, the ground reflection and ionosphere refraction points nearest the receiver could be considered the locations of *virtual transmitters* (figure 1-8). The concept of virtual transmitters was introduced in [Reeve21].

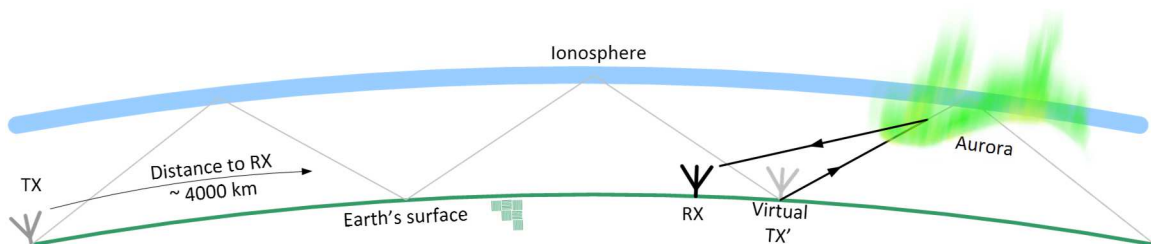


Figure 1-8 ~ 3-hop propagation path from a transmitter Tx to a point in the aurora beyond the receiver Rx. The 3rd hop is shown with a virtual transmitter TX' at the ground reflection point a little north of the receiver but other locations both north and south may be possible. The virtual transmitter is used to explain how signals from the distant WWVH transmitter can be reflected off the aurora and detected at Anchorage. The reflection points in the aurora are wherever the propagation geometry provides a common plane holding the virtual transmitter, receiver and aurora field aligned electron columns and the incident radio wave is near a right-angle to the magnetic field. The reflected signal may be refracted from the F-region on its way back to the receiver rather than direct as shown here.

Examination of the path's geometric characteristics for various ionosphere reflection heights (table 1-1) indicates that 1-hop paths from WWVH to aurora radio reflection regions are unlikely except, possibly, under exceptional propagation conditions. The 2-hop paths place a virtual transmitter Tx' more than 2300 km from the aurora radio reflection region and also are unlikely.

Table 1-1 ~ Propagation path geometric characteristics between a transmitter at WWVH and an aurora radio reflection region 1000 km north of Anchorage for F-region ionosphere heights $H = 250, 300$ and 350 km. Segment distances are straight line distances in km. Hop angles are elevations above the horizon in $^{\circ}$. The calculations assume: (1) Earth radius of 6370 km ($K = 1$); (2) Equal distances between ground reflections and ionosphere refraction regions; and (3) Propagation follows great circle paths (no off-path or tilted-path reflections or refractions). For multi-hop paths, it is assumed that the refraction heights are identical on all hops. Note: For the cases indicated by *, the minimum height required for 1-hop refraction is 595 km. All distance and angle calculations are according to [{Reeve-IDC}](#).

Path	Great Circle Distance	1-hop Angle	Segment distance	2-hop Angle	Segment distance	3-hop Angle	Segment distance	4-hop Angle	Segment distance
H = 250 km									
WWVH → ARR	5400	< 0	*	4.2	1396	11.2	950	16.9	732
H = 300 km									
WWVH → ARR	5400	< 0	*	6.1	1411	14.0	968	20.4	753
H = 350 km									
WWVH → ARR	5400	< 0	*	8.0	1428	16.6	988	23.7	776

The 3- and 4-hop propagation modes are more favorable because they involve distances under 2000 km from a virtual transmitter to the aurora radio reflection region and their hop angles are more in line with providing the required propagation path geometry. Since most aurora reflections are received at night after the ionosphere’s D-region has disappeared, absorption is minimal, making higher mode paths possible.

The reflected signal back to the receiver could follow a direct path but also could involve F-region ionospheric refraction as well. Referring to figure 1-9, for a reflection altitude of 100 km and a distance of 1000 km from the aurora to the receiver, the elevation angle at Anchorage of the propagation is 1° , only slightly above the horizon. Such a reflection point 1000 km north of Anchorage is above the north coast of Alaska at approximate latitude 70° N and within the auroral oval. It was previously shown (section 1-3) that the magnetic field’s dip angle is close to 81° in that reflection region so a propagation path elevation angle near 19° is preferred. The low elevation angles for a direct path do not provide the preferred geometry but that does not mean that reception of the reflections is precluded.

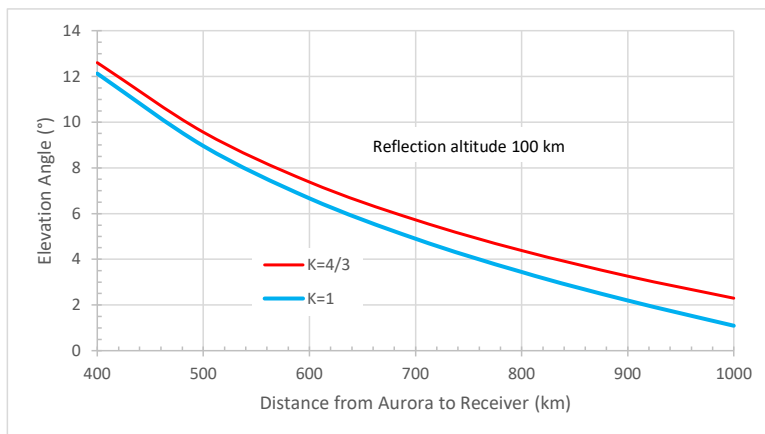


Figure 1-9 ~ Calculated elevation angles at Anchorage for an aurora reflection region at 100 km height above ground and distances of 400 to 1000 km. Two effective Earth radius factors are plotted: $K = 1$ (Earth radius 6470 km) and $K = 4/3$ (Earth radius 8493 km), the latter often used in radio path studies to account for atmospheric refraction. Calculations are according to [\[Reeve-IDC\]](#).

Daily, seasonal, yearly and long-term variations: Aurora is not normally visible in Alaska during summer because of the relatively long daylight hours, especially at higher latitudes. However, as mentioned previously, visible aurora is not necessary for aurora radio to be detected. Because aurora is related to geomagnetic activity that is

controlled by the solar wind, it is expected that short-term, seasonal, yearly and long-term variations in the detection of aurora radio reflections follow similar variations in solar activity.

Solar activity follows well-known patterns. For example, solar features such as sunspots and coronal holes, both of which can produce geomagnetic disturbances, may persist for more than one solar rotation. The Sun rotates in a nominal 27 days, so geomagnetic disturbances and aurora associated with persistent solar activity may repeat at that interval. Active regions on the Sun can produce flares and other disturbances that affect the geomagnetosphere during the almost 2-week period when the regions are visible from Earth. Longer term, the 11-year sunspot cycle produces more geomagnetic disturbances and aurora around solar maximum than around solar minimum.

Visible aurora most often occurs around *local solar midnight*. Local solar midnight is the time when the Sun is aligned with a point on the opposite side of Earth from the observation point (figure 1-10). Solar time is not necessarily the same as local time due to time zones and daylight saving time. For example, solar noon and midnight at Anchorage are 2200 and 1000 UTC, respectively. The corresponding local times are 1:00 pm or 2:00 pm for local noon and 1:00 am and 2:00 am for local midnight, depending on daylight saving time.

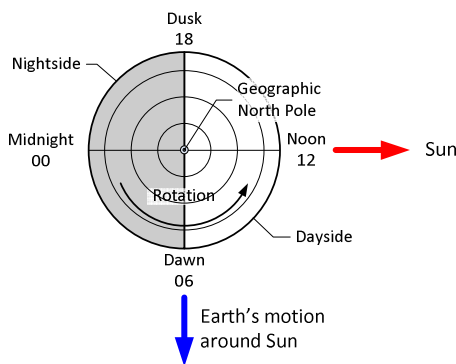


Figure 1-10 ~ Concept of local solar time in the northern hemisphere. When the Sun is on the same plane as the location in question and the geographic north pole, the time is *local solar noon* (12). Twelve hours later, that location, the geographic north pole and Sun are again on the same plane and the time is *local solar midnight* (00). Local solar time is close to but not the same as *magnetic local time* (MLT). MLT is based on the geomagnetic pole location and not the geographic pole.

1-5. Instrumentation

Instrumentation: The radio instrumentation originally was setup during summer 2014 and has operated almost continuously since then with some hardware updates along the way. The 3-axis SAM-III magnetometer originally was installed in fall of 2010 and has operated without significant interruption since then (the SAM-III replaced a 1-axis SAM originally installed in spring 2008). Both the receiver and magnetometer instruments are setup to record data continuously.

A block diagram of the receiver and antenna system at Anchorage shows the setup (figure 1-11). Because of the equipment integration and multi-use configuration of the Anchorage observatory, equipment may have been temporarily repurposed for a different project, leaving some relatively short gaps in the records for 2020.

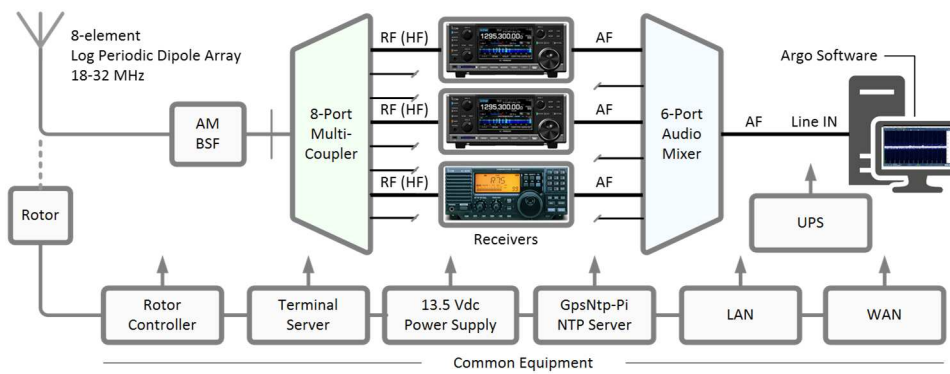


Figure 1-11 ~ Receiver and antenna system block diagram. PC timing is controlled by two GPS receiver-based network time protocol (NTP) servers. Common equipment is shared with other observatory equipment. The antenna usually was rotated to point at WWV on a true bearing of 107° but has sidelobes pointed north-south.

The receivers generally are tuned to fixed frequencies for long time periods. The WWV and WWVH transmitters at 15 and 20 MHz and WWV at 25 MHz are used exclusively, but the observations in 2020 were made with only one R-75 receiver tuned to 15 MHz. However, in late 2020 two R-8600 receivers were added and used throughout 2021 and later.

The R-75 receivers are equipped with the optional CR-282 high-stability crystal, which significantly reduces oscillator drift and stabilizes the signal trace on the Argo software. The R-8600 receivers are factory-equipped with high-stability oscillators. Although the R-8600 receivers may be operated with an external 10 MHz precision frequency reference source, I found they are very stable and an external reference is unnecessary.

The demodulated audio output from each receiver is fed through a 6-channel analog stereo audio mixer, one receiver per channel, and then to the PC soundcard Line In jack. The audio mixer allows up to six receivers to share one soundcard input. I usually operated the receivers in lower sideband (LSB) mode with the AGC turned off, and I usually tuned the receiver 1000 Hz above the RF carrier frequency. The offset tuning with LSB provides a 1000 Hz beat note, and it is this beat note that is processed by the Argo software, not the carrier itself. When running more than one receiver, I tuned the others to a different offset above the carrier frequency so that they displayed distinctly different traces on the Argo waterfall. I usually operated the receivers with their RF gain set to maximum and their internal preamplifier or attenuator turned off.

The Argo software used with the receivers originally was developed for very low speed, weak signal, digital communication modes but is used here to display the demodulated HF carriers in a 42.75 Hz frequency span (± 21.375 Hz from center). The input to Argo is a digitized demodulated signal, so only amplitude information may be derived from it (no phase). Argo processes the digitized signal using the Fast Fourier Transform (FFT) and displays the amplitude of each FFT bin as a pixel on the frequency scale. The FFT bin size for the setup used here is 91.55 mHz, and the frequency scale is 467 pixels high.

The Argo horizontal scale is 890 pixels wide. The total span shown on the time scale is 13.38 min, so the resolution is 0.9 s pixel^{-1} . Argo automatically produces periodic screenshots of the spectra as Portable Network Graphics (.png) files but does not save the data in any other form. The actual amplitude-frequency-time value of any given pixel is only accessible through image pixel analysis, and that was not done here. Argo saves the images to an archive with a sequence number or time-stamp. The images also are sent in near real-time to my website and displayed at [ReeveArgo](#). Image file sizes vary from around 20 kB to 200 kB depending on the

displayed activity. The software runs continuously, producing a little more than 100 image files per day. Argo images are discussed below.

The SAM-III magnetometer hardware (figure 1-12) produces data at 10 s intervals for each of the three geomagnetic components X (north-south), Y (east-west) and Z (vertical) according to the Geographic Reference System. The associated SAM_VIEW software collects and saves the data in real-time in tabulated comma separated variable ASCII text files. SAM_VIEW also plots the data on a magnetogram and displays it on an observatory PC in real-time. The software simultaneously produces .png images of the magnetograms for archive purposes. All files are produced on a 24 h basis (one data and image file each day) and time- and date-stamped accordingly. The SAM-III magnetogram images are sent for display to a dedicated page on my website {[ReeveSAM](#)}. The SAM_VIEW magnetograms are discussed below.

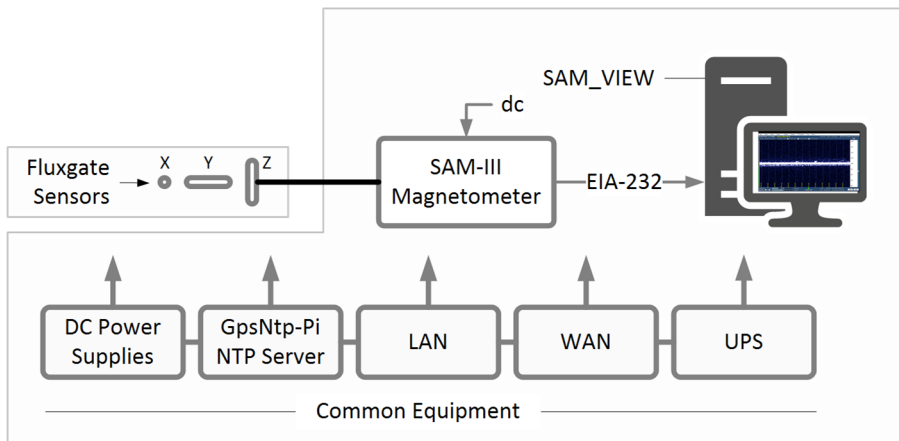


Figure 1-12 ~ System block diagram for the 3-axis SAM-III magnetometer at Anchorage including the common equipment shared across the observatory. The SAM-III consists of a controller and three sensors, one for each magnetic component X, Y and Z in the Geographic Coordinate System. The sensors are buried about 1 m below the ground surface to reduce temperature effects.

Correlation of spectra and magnetic activity: The detections of aurora radio reflections are recorded on horizontal waterfall spectrograms (figure 1-13) and the times are compared to magnetic activity recorded on magnetograms (figure 1-14). The two figures explain the elements of the plots. The trace in the Argo plots shows the demodulated RF carrier. The receiver usually is set to LSB and tuned 1000 Hz above the carrier frequency. For example, for a 15 MHz carrier, the receiver is tuned to 15.001 000 MHz.

When a strong carrier is received via a direct, ionospheric path from the transmitter to the receiver (not reflected by aurora) and demodulated, it is recorded as a bright, straight, horizontal trace at 1000 Hz. Weak signals received via a direct path are not bright but still are straight and horizontal. Doppler frequency shifts during reflections are shown as deviations from 1000 Hz on the Argo plot and may be bright, slanted traces, irregular traces or diffuse, wavy traces.

Interpreting the spectra and magnetograms is an important part of the observations, and it is possible to misinterpret them. However, the aurora radio reflections have specific time and spectral characteristics that do not fit with other propagation phenomena observed at Anchorage. For example, the aurora radio reflections often occur around local solar midnight, indicate rapid and significant frequency shifts and are well correlated in time with rapid magnetic field changes shown on the magnetograms.

It is observed that sunset along the path from the transmitter to the receiver often introduces radio propagation effects including frequency shifts that look similar to some aurora radio reflections. These are particularly visible

on the east-west WWV path along which the solar terminator travels during sunset. The frequency deviations are due to electron-ion recombination in the ionosphere that causes somewhat rapid changes in the ionosphere's apparent height and, thus, the wave number along the radio propagation path to Anchorage from the transmitters. The sunset effects usually result in wide diffuse traces with comparatively slow frequency variations and not the bright slanted and rapidly varying traces seen in aurora radio reflection plots. To guard against false detections of aurora reflection, Argo plots around local sunset were generally excluded from the analyses even though some showed a familiar spectral signature.

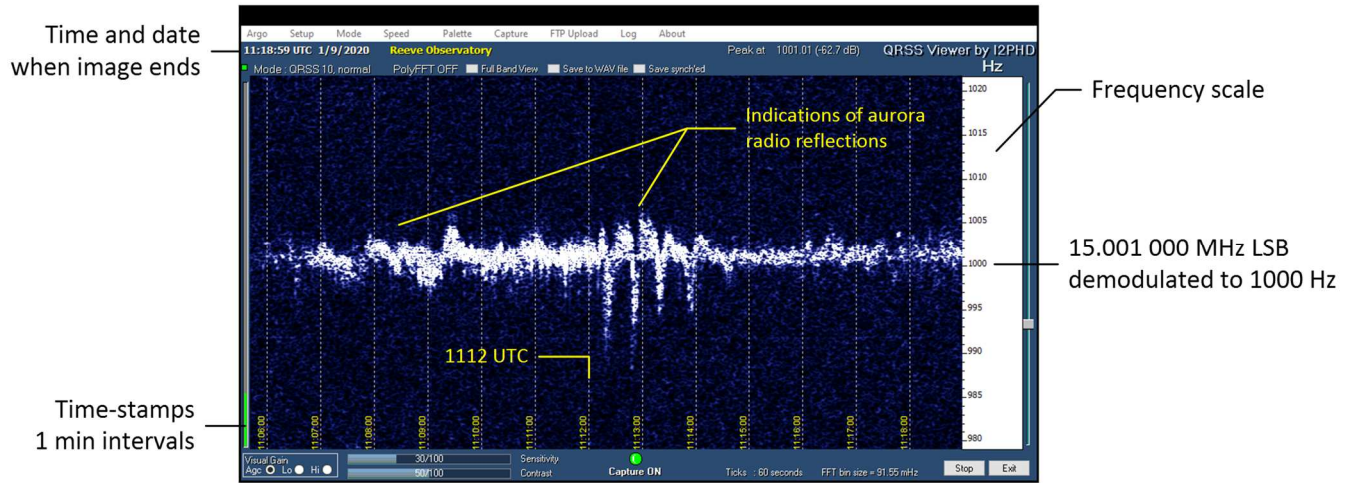


Figure 1-13 ~ Annotated Argo image pointing out the time-stamps, frequency scale and ending time and date for the plot. This example from 9 January 2020 is for the time span 1106 to 1119 UTC. An example of aurora radio reflections is indicated by the white, rapidly varying trace starting near the left end of the plot. Not visible here but occasionally seen on other Argo plots are spurious signals of unknown origin that slowly drift through the spectrum. They are easily recognized and usually do not obscure spectra of interest. Signals that follow a direct path from the transmitter to the receiver (not reflected from aurora) also may be seen but these usually are thin, straight, horizontal lines.

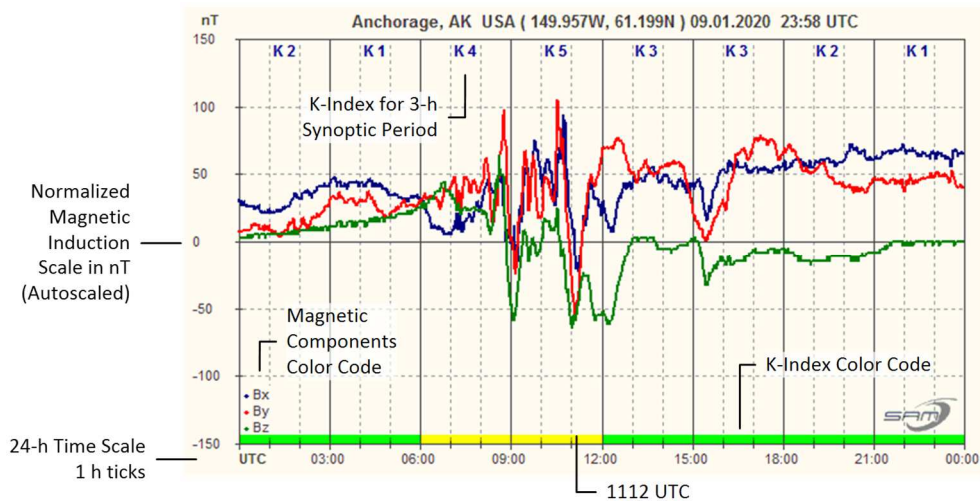


Figure 1-14 ~ Annotated SAM-III magnetogram. The time scale is at the bottom in UTC and the normalized magnetic flux density (magnetic induction) is on the left vertical scale. Note that the displayed magnetic induction values are normalized to the values at 0000 UTC, so the plot shows changes with respect to that time. The plot shows other SAM-III features including the K-index for each 3-h synoptic period. This example is for the same day as the example Argo image shown

above and has a matching time mark at 1112 UTC. Note the time-correspondence between the Argo signal trace variations and the rapid changes in the measured magnetic field. The overall aurora reflection event started around 0700; see Part 2.

Keograms: In addition to the data produced by instruments in the Anchorage observatory, I also used certain professional data to aid in the determination of auroral activity. In particular, I compared candidate geomagnetic and radio propagation disturbances shown by my instrumentation to data from the *Time History of Events and Macroscale Interactions during Substorms* {THEMIS} program. These data included:

- ⚙ *Ground Mag* and subset *High-Lat H* for ground magnetometer data;
- ⚙ *Orbits: Multi-Mission* for spacecraft orbits to determine if in the magnetotail;
- ⚙ *All-sky Imager* and subsets *Keogram*, *Summary* and *Mosaic* for all-sky imager data.

Of these data, all-sky images and keograms produced from those images were the most usable (figure 1-15). Rather than 360° views from horizon-to-horizon, as in the original all-sky images, a keogram uses a snapshot of a small portion of the all-sky data and combines the snapshots in a time series from dusk to dawn along the horizontal axis. The latitude angle from the southern horizon at the bottom to northern horizon at the top is along the vertical axis. The zenith, or directly overhead, is at the midpoint between the keogram top and bottom. Bright areas usually represent aurora, but the Moon and spurious lights can enter some images. The THEMIS keograms from each site are stacked from east to west with the farthest west (latest) site at the top. See acknowledgments in section 1-7.

The THEMIS all-sky cameras only operate during darkness; therefore, no images were available from the Alaska and western Canada sites during the summer months May through July and almost all of August due to the long daylight hours. Also, some days with aurora radio were cloudy at the THEMIS sites or a site was out of service, so no keograms were available for comparison on those days. Even though all-sky images were produced at many sites in Canada, in addition to those in Alaska, none of the Canadian sites were examined except Whitehorse and Inuvik because the other sites are too far east to indicate possible auroral activity above northern Alaska at the times of interest.

Although keograms were useful and are included in Part 2 when available, they were not used as go/no-go flags of radio aurora because early investigations noted that visible and radio aurora do not always occur together.

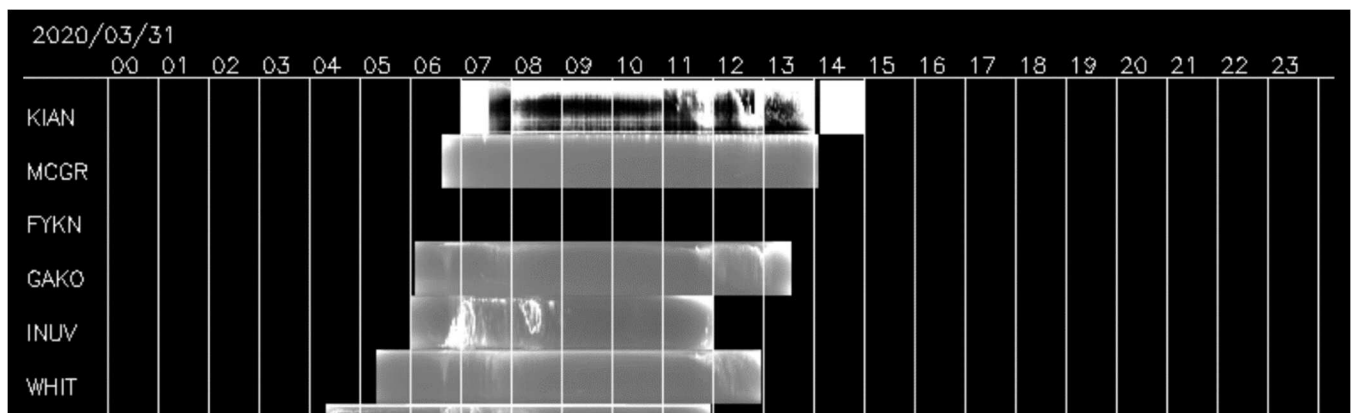


Figure 1-15 ~ Example THEMIS keograms from six sites for 31 March 2020 (date is shown in the upper-left corner). The UTC time of day is along the top horizontal axis. The sites are shown on the left: Kiana (KIAN), McGrath (MCGR), Fort Yukon (FYKN), Gakona (GAKO), Inuvik (INUV) and Whitehorse (WHIT). All sites except INUV and WHIT are in Alaska (the Alaska site

FYKN is off-the-air in this image). INUV and WHIT are in western Canada. The farthest east, or earliest, site is at the bottom and farthest west, or latest, at the top. See text for additional explanation of the keogram. Image source: See acknowledgments.

1-6. References and Weblinks

Technical References:

- [Booker] Booker, H., Gartlein, C., and Nichols, B., Interpretations of Radio Reflections from the Aurora, Journal of Geophysical Research, Vol. 60, No., 1, March 1955
- [Currie] Currie, B., Forsyth, P., Vawter, F., Radio Reflections from Aurora, Journal of Geophysical Research, Vol. 38, No. 2, June 1953
- [Forsyth56] Forsyth, P., Vogan, E., The Frequency Dependence of Radio Reflections from Aurora, Journal of Atmospheric and Terrestrial Physics, Vol. 10, 1957
- [Forsyth60] Forsyth, P., On the Geometry of Radio Reflections from Aurora, Canadian Journal of Physics, Vol. 38, 1960
- [Forsyth63] Forsyth, P., Reflection Mechanisms for Radio Aurora, Planetary and Space Science, Vol. 10, 1963
- [Hultqvist] Hultqvist, B., Egeland, A., Radio Aurora, Space Science News, D. Reidel Publishing Co., 1964
- [Knipp] Knipp, D., Understanding Space Weather and the Physics Behind It, Space Technology Series, US Department of Defense and NASA, 2011
- [Stoffregen] Stoffregen, W., Radio Reflections on Low Frequencies from 70-90 km Height During Intense Aurora Activity, Research Notes, December 1957
- [Moorcroft-1] Moorcroft, D., Models of Auroral Ionization, Part I, Applications to Radio Observations of Aurora, Canadian Journal of Physics, Vol. 39, 1961
- [Moorcroft-2] Moorcroft, D., Models of Auroral Ionization, Part I, Auroral Ionization Models and Their Radio-Reflection Characteristics, Canadian Journal of Physics, Vol. 39, 1961
- [Seki] Seki, K., et al, A Review of General Physical and Chemical Processes Related to Plasma Sources and Losses for Solar System Magnetospheres, Space Science Reviews, August 2015, DOI 10.1007/s11214-015-0170-y

Other References:

- [Houston] Houston, Edwin J., The Elements of Physical Geography for the use of Schools, Academies, and Colleges, Eldredge & Brother, 1891
- [Hunsucker] Hunsucker, R. and Hargreaves, J., The High-Latitude Ionosphere and Its Effects on Radio Propagation, Cambridge University Press, 2003
- [Reeve15-1] Reeve, W., Sudden Frequency Deviations Caused by Solar Flares: Part I ~ Concepts, 2015, available at:
http://www.reeve.com/Documents/Articles%20Papers/Propagation%20Anomalies/Reeve_SuddenFreqDevConcepts_P1.pdf
- [Reeve15-2] Reeve, W., Sudden Frequency Deviations Caused by Solar Flares: Part II ~ Instrumentation and Observations, available at:
http://www.reeve.com/Documents/Articles%20Papers/Propagation%20Anomalies/Reeve_SuddenFreqDevMeas_P2.pdf
- [Reeve21] Reeve, W., HF Meteor Trail Reflections Observed at Anchorage, Alaska USA, available at:
https://www.reeve.com/Documents/Articles%20Papers/Reeve_MeteorRadioObsrv.pdf

{[Reeve-IDC](#)} Ionosphere-Distance Calculations, 2020, available at:
http://www.reeve.com/Documents/Articles%20Papers/Reeve_Ionosphere-DistanceCalc.pdf
[QST26] Sutton, W., Aurora and Its Effects Upon Radio Signals, QST, ARRL, October 1926

Weblinks:

{[Argo](#)} <https://www.i2phd.org/argo/index.html>
{[GCMaP](#)} <http://www.gcmap.com/mapui?P=FNL-anc-bkh>
{[IRI](#)} https://ccmc.gsfc.nasa.gov/modelweb/models/iri2016_vitmo.php
{[Oval](#)} <http://broadcast.homestead.com/aurora.gif>
{[ReeveArgo](#)} http://www.reeve.com/Meteor/Meteor_simple.html
{[ReeveSAM](#)} http://www.reeve.com/SAM/SAM_simple.html
{[SWPC-Oval](#)} <https://www.swpc.noaa.gov/products/aurora-30-minute-forecast>
{[THEMIS](#)} <http://themis.igpp.ucla.edu/summary.php?year=2020&month=01&day=01&hour=0024&sumType=asi&type=summary>

1-7 Acknowledgments:

The author is grateful for review comments provided by Doğacan Su Öztürk of the University of Alaska Fairbanks – Geophysical Institute. The author also acknowledges NASA contract NAS5-02099 and V. Angelopoulos for use of data from the THEMIS Mission, and S. Mende and E. Donovan for use of the ASI data, the CSA for logistical support in fielding and data retrieval from the GBO stations, and NSF for support of GIMNAST through grant AGS-1004736.

HF Aurora Reflections Observed at Anchorage, Alaska USA

Part 2 ~ Observations

2-1. Description

Simple criteria were used to find instances of aurora radio reflections in the observation data: (1) Rapid frequency shifts on time scales of seconds or minutes visible in the Argo horizontal waterfall spectra; and (2) Rapid changes in the magnetic field at the same time as the frequency shifts.

The observations were made in 2020 during the first 12 months of solar cycle 25. The early part of any solar cycle typically is relatively quiet in terms of HF radio propagation effects from magnetic disturbances. Nevertheless, every month of this study, except December, showed significant geomagnetic activity ($K\text{-index} \geq 4$) with the potential to produce aurora and aurora radio reflections. All months produced reflections except December; the lack of aurora radio in December may have been the relatively low geomagnetic activity or poor propagation conditions in which no signals reached far enough north to be reflected or, if reflected, the propagation geometry was not conducive to reception at Anchorage.

It is possible that some candidate spectra reviewed in the 2020 data were due to sporadic-E (Es) propagation but this propagation mode is not expected to show the rapid Doppler frequency shifts in the observations discussed here. Also, traveling ionospheric disturbances (TID) and ionospheric patches and blobs could cause similar spectra but these probably are not correlated with magnetic field disturbances as are aurora radio reflections.

The Argo images shown in this section represent only a fraction of the images from 2020 that show possible aurora radio reflections. A total of the almost 43 thousand Argo images were viewed. The list by month shows the number of days in which candidate aurora radio reflections were observed (table 2-1). A summary of the images shown in this section is given below (table 2-2). The Argo images, magnetograms and keograms (when available) are shown in chronological order along with brief descriptions.

Time references:

- ⚙ Time of local solar midnight was $1000 \text{ UTC} \pm 10 \text{ min}$ at Anchorage from 1 January to 31 December 2020.
- ⚙ From 8 March to 1 November, 2020, local time (Alaska Daylight Saving Time, AKDST) = UTC-8; from 2 November to 7 March, local time (Alaska Standard Time, AKST) = UTC-9.

Keograms: Keograms were used for reference at times of possible radio aurora; they are shown in section 2-2 below with the Argo spectra and SAM-III magnetograms. The magnetogram and keogram image sizes are adjusted so that their time scales match as an aid in keogram interpretation. Keogram site key: Kiana (KIAN), McGrath (MCGR), Fort Yukon (FYKN), Gakona (GAKO), Inuvik (INUV), Whitehorse (WHIT), and Fort Simpson (FSIM).

Variability: Several of the radio aurora observations at Anchorage appear to follow a pattern similar to visible aurora, which start with a relatively quiet condition, evolve to a more active condition and return to a quiet condition. This pattern is called a *substorm* and may occur a few times a night when aurora is active. Visible aurora normally cannot be seen at the Anchorage Radio Observatory because of light pollution, so it was not possible to compare visual aurora with the radio data. Also, since observations of aurora radio at Anchorage

depend on favorable propagation conditions, this pattern, if it existed, was not always apparent in the Argo spectra.

Table 2-1 ~ Number of days with observations of aurora radio reflections at Anchorage

Month	Number of days
January	5
February	5
March	12
April	13
May	6
June	7
July	5
August	6
September	13
October	3
November	1
December	0
Total	76

Table 2-2 ~ Summary of Argo images shown in this section. Time (solar) = Time (UTC) – 10 h.
 Bold text in the Sector column indicates event was within 1 hour of a sector boundary

Figure	Date (UTC)	Time (UTC)	Time (Solar)	Argo Image	Freq. (MHz)	Sector
2-1.a	9 Jan 2020	0654-0742	2054-2142	48 min, splice 4	15	Dusk-Midnight
2-1.b	9 Jan 2020	1106-1130	0106-0130	24 min, splice 2	15	Midnight-Dawn
2-2	22 Jan 2020	0954-1019	2354-0019	25 min, splice 2	15	Midnight
2-3	21 Mar 2020	0601-0720	2001-2120	80 min, splice 6	15	Dusk-Midnight
2-4	29 Mar 2020	0828-0907	2228-2307	39 min, splice 3	15	Dusk-Midnight
2-5	30 Mar 2020	0734-0747	2134-2147	13 min	15	Dusk-Midnight
2-6	1 Apr 2020	0816-0841	2216-2241	25 min, splice 2	15	Dusk-Midnight
2-7	15 Apr 2020	0620-0712	2020-2112	52 min, splice 4	15	Dusk-Midnight
2-8	11 May 2020	0823-0835	2223-2235	26 min, splice 2	15	Dusk-Midnight
2-9	2 Jun 2020	0351-0510	1751-1910	78 min, splice 6	15	Dusk
2-10.a	5 Jul 2020	0519-0558	1919-1958	39 min, splice 3	15	Dusk-Midnight
2-10.b	5 Jul 2020	0759-0918	2159-2318	78 min, splice 6	15	Dusk-Midnight
2-11	24 Jul 2020	0843-1122	2243-0122	156 min, splice 12	15	Midnight
2-12	12 Sep 2020	0741-0902	2141-2302	91 min, splice 7	15	Dusk-Midnight
2-13	24 Sep 2020	0702-0915	2102-2315	130 min, splice 10	15	Dusk-Midnight
2-14	28 Sep 2020	0545-0838	1945-2238	156 min, splice 12	15	Dusk-Midnight
2-15	30 Sep 2020	0825-0918	2225-2318	53 min, splice 4	15	Dusk-Midnight
2-16	5 Oct 2020	1501-1540	0501-0540	39 min, splice 3	15	Midnight-Dawn
2-17	17 Oct 2020	0554-0807	1954-2207	133 min, splice 10	15	Dusk-Midnight
2-18	22 Nov 2020	0759-0837	2159-2237	39 min, splice 3	15	Dusk-Midnight

Geomagnetic Disturbances: Disturbances in Earth’s magnetic field correlate well with aurora. It is apparent from the observations that the rates of change (*gradient*) of the magnetic field are more important to aurora radio detections than the magnitudes of the magnetic field changes. The K-index, which indicates the peak-to-peak change in the magnetic field H-component in a 3 hour synoptic period, does not appear to be well correlated with aurora radio. In other words, a high K-index did not necessarily mean a high occurrence of aurora radio. Several instances of aurora radio were observed when the K-index was relatively low (K3-K4) but the magnetic field changes were rapid.

Demodulated Audio: I often monitored the demodulated audio when the aurora radio reflections occurred early enough in the evening, but I did not routinely record it. Generally, the signals were very weak. The audio was characterized by rapid variations (called *flutter* or *stutter*) with a rapid hash- or buzz-like sound. Sometimes, it was impossible to verify the source as WWV or WWVH. However, if reflections and direct path signals were being received, I could discern the female voice announcements from WWVH and the male voice from WWV.

Detection Times: Most aurora radio reflections were detected within 4 h of 1000 UTC, corresponding to local solar times 8:00 pm to 4:00 am. Generally, reflection events spanned two or more 13 min Argo images, and many images in this section are spliced together to show the entire event. Some events spanned 3 h. A few daytime reflections and reflections outside this time range were detected. Most reflections were detected while Anchorage was in the dusk-midnight sector (between sunset and local solar midnight). There were some technical problems during most of May, so even if aurora radio reflections existed, they were not recorded.

Spectral Characteristics: Two types of spectral signatures are seen in the Argo plots of aurora radio reflections. One, which I call *discrete* aurora radio, is seen as bright, thin lines with rapid frequency shifts that often cover the full 40 Hz frequency span of the Argo plots. Another is a bright but diffuse trace with rapidly drifting frequencies and is called *diffuse* aurora radio. The frequency shifts of the diffuse type usually are not as great as the discrete type. Both types sometimes appear during any given time period but usually not simultaneously. Note that there are discrete and diffuse visible aurora types but it is not known if there is any relationship with radio aurora of the same name.

Doppler Frequency: Aurora radio reflections are heavily Doppler frequency shifted, indicating rapid changes in the ionization in the reflection regions. This could mean the electron clouds themselves moved or the clouds remained stationary but the *ionizing agency* moved. Strong winds are known to exist at the altitudes in question but it is impossible to determine the reason for the Doppler shifts without specialized radar. The spectra imaged by the Argo setup used in 2020 were limited to a displayed frequency span of 40 Hz. Therefore, Doppler frequency shifts exceeding this limit were not recorded.

The observed Doppler shifts and equation (7) in Part 1, can be used to make a 1st-order estimate of the radial velocity for the simple case where the reflection region is assumed to be moving directly along the bisector between the transmitter and receiver. In this case, $\delta = 0^\circ$ or 180° for toward and away from the transmitter and receiver, respectively. The maximum observed Doppler frequency was limited to ± 20 Hz because of the software setup, and that will be used in this calculation (note that the Argo plots shown in this part indicate that higher values were possible). Assuming the bistatic angle θ is small, no more than a few degrees, and a wavelength of 20 m (15 MHz), solving equation (7) for the velocity gives

$$v = \frac{F_D \cdot \lambda}{2} \left/ \left[\cos(\delta) \cdot \cos\left(\frac{\theta}{2}\right) \right] \right. = \frac{20 \cdot 20}{2} \left/ (1 \cdot 1) \right. = 200 \text{ m s}^{-1}$$

The above result is for the situation where the reflection region is moving toward the transmitter and receiver. The magnitude is consistent with the early investigations discussed in Part 1. If the reflection region is assumed to be moving away from the transmitter and receiver, the velocity will be the same magnitude but negative.

Doppler Polarity: The spectral traces on many of the Argo plots indicate a bias toward negative Doppler frequency shifts; that is, the negative shifts generally were higher or occurred more often than the positive shifts. A negative shift (lower demodulated frequency) indicates the reflective object is moving away from the transmitter and receiver, both of which are fixed. The early investigations showed that, in general, the sign of the velocity was positive before midnight. As previously mentioned, most detections in 2020 were made before midnight but the frequency shifts were biased toward negative values, contrary to the results from early investigations (see section 1-2).

2-2. Spectral Images, Magnetograms and Keograms

All Argo images have a vertical frequency span of 40 Hz

All spectra show a demodulated 15 MHz carrier with the receiver tuned to 15.001 000 MHz in LSB mode

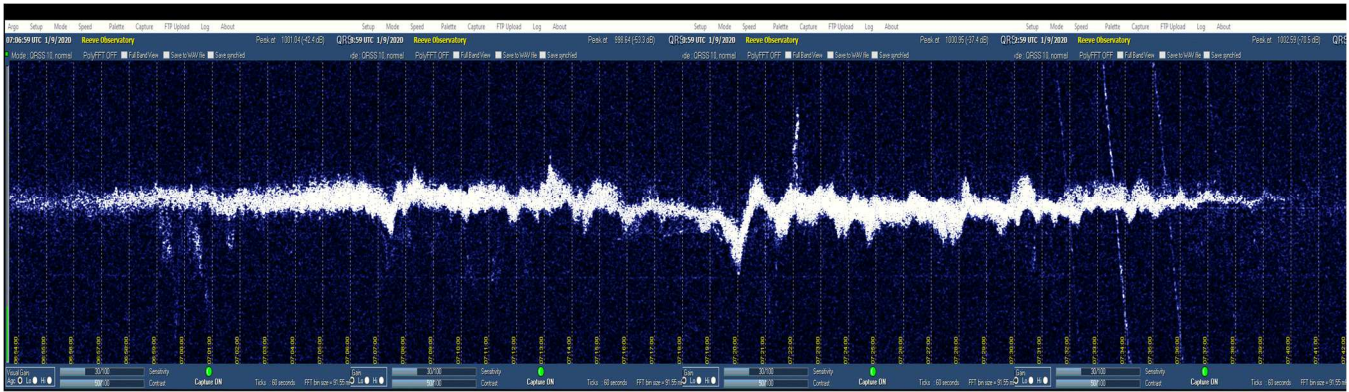


Figure 2-1.a ~ 9 January 2020 from 0654 to 0742 UTC. Image has been stretched vertically to enhance the frequency shift. Composite of four 13-minute images spliced together corresponding to a 52-minute portion of the 24-h magnetogram below. The K-Index during the 0600 to 0900 synoptic period reached only K4 but the magnetic gradient was high. The faint slanted trace on the right is spurious. Reference: SS 0107 : SR 1904 UTC, LT=UTC-9

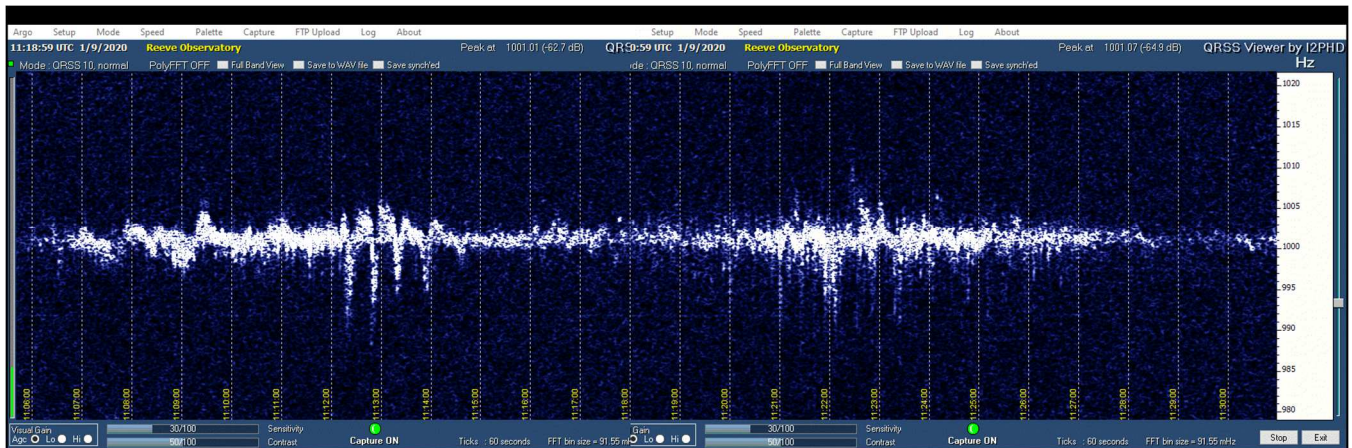


Figure 2-1.b ~ 9 January 2020 from 1106 to 1130 UTC, approximately 4 hours after the previous plot. Composite of two 13-minute images corresponding to a 26-minute portion of the magnetogram below. The K-index reached K5 during the interval. The periodic structures have a peak-peak frequency shift of about 20 Hz. Reference: SS 0107 : SR 1904 UTC, LT=UTC-9

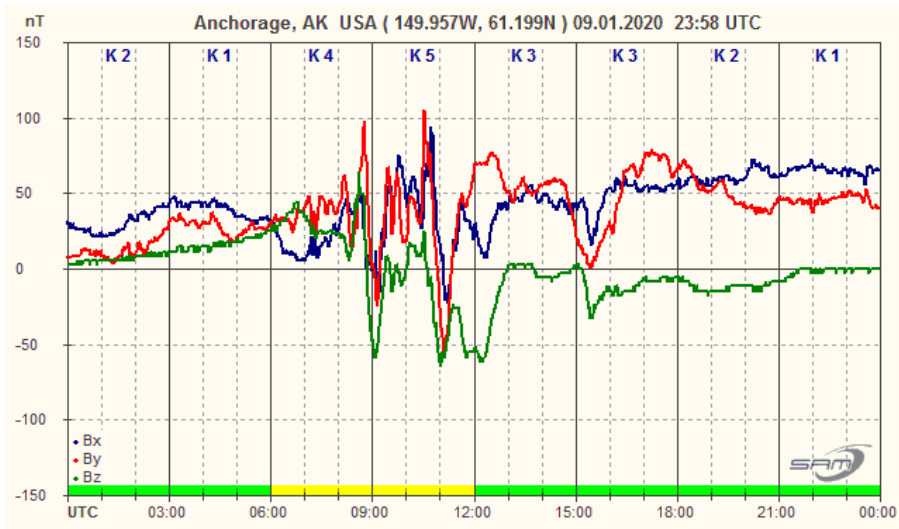


Figure 2-1.c ~ Magnetogram for the 24-hour period on 9 January 2020. Note that the B_y component (east-west) starts pulsing around 0630 with rapid upward and downward swings just before 0700 when B_x and B_z (blue and green traces, respectively) start deflecting. The magnetic disturbance continues through about 1200, resulting in a K-Index of 5 for the 0900 to 1200 synoptic period. This series of disturbances straddles local solar midnight (1000 UTC).

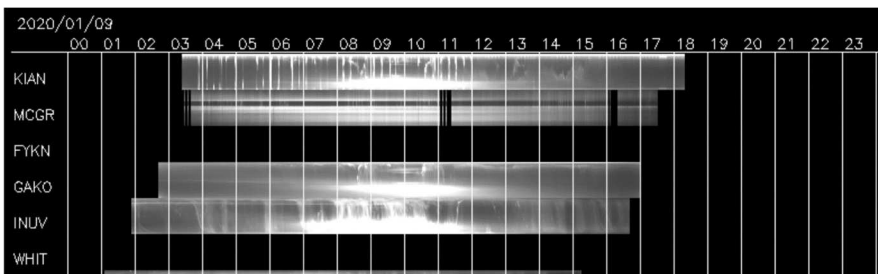


Figure 2-1.d ~ Keogram of all-sky images for 9 January 2020. Aurora activity is apparent during both periods shown on the above Agro plots.

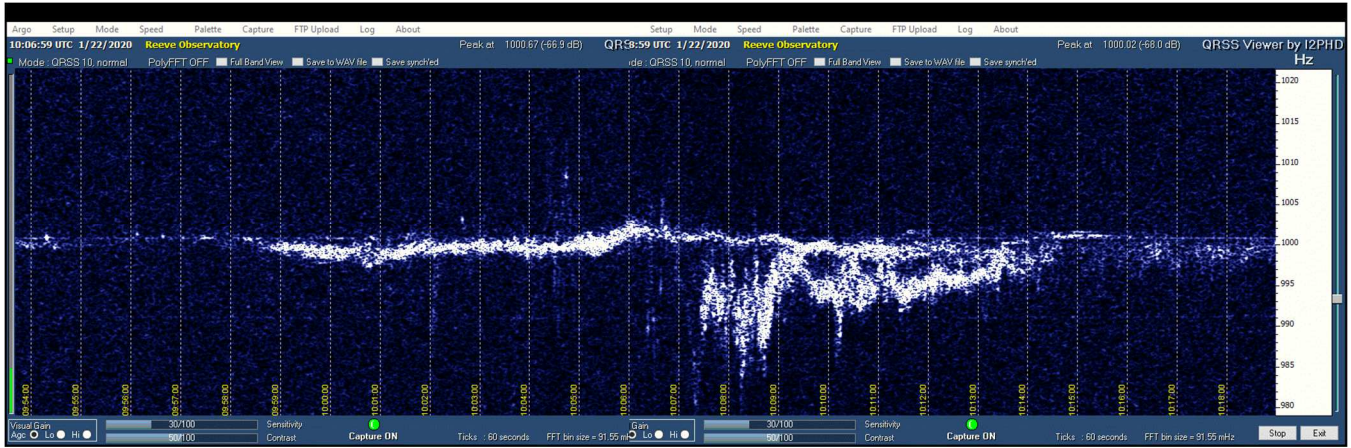


Figure 2.2.a ~ 22 January 2020 from 0954 to 1019 UTC. Composite of two images corresponding to a 25-minute portion of the magnetogram below. The slightly meandering trace along the center may be a direct path signal. About midway, another trace overlays the meandering trace that shows predominantly negative frequency shift and lasting 7-8 min. Reference: SS 0139 : SR 1841 UTC, LT=UTC-9

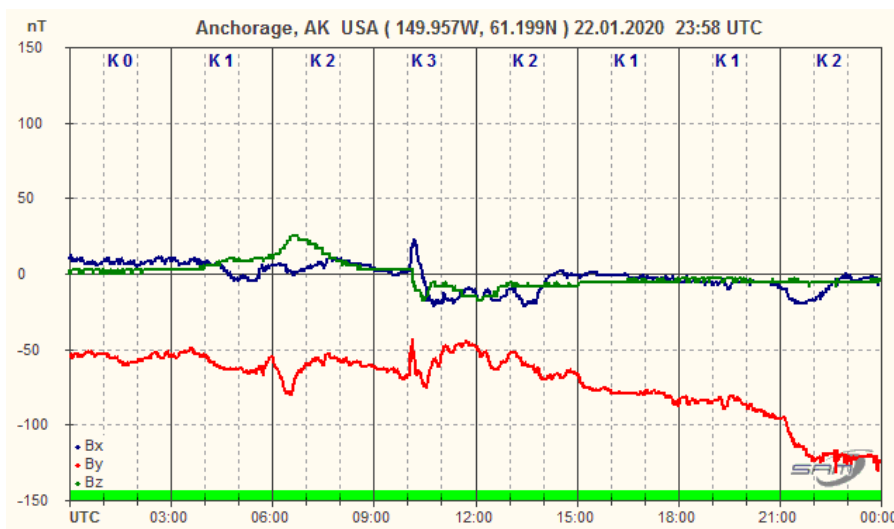


Figure 2-2.b ~ Magnetogram for the 24-hour period on 22 January 2020. The Argo plot above corresponds to the small but rapid geomagnetic disturbance in B_y and B_z (red and green traces, respectively) at 1000 and lasting about 0.5 hour. Note that the K-index is only K3 – an *unsettled* condition.

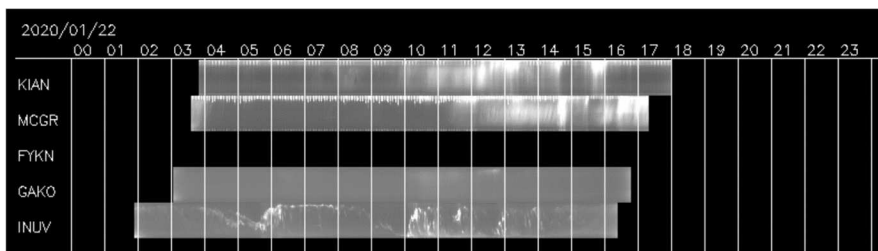


Figure 2-2.c ~ Keogram of all-sky images for 22 January 2020. The westward site KIAN shows only very weak aurora at 1000 but the eastward site INUV shows distinct activity.

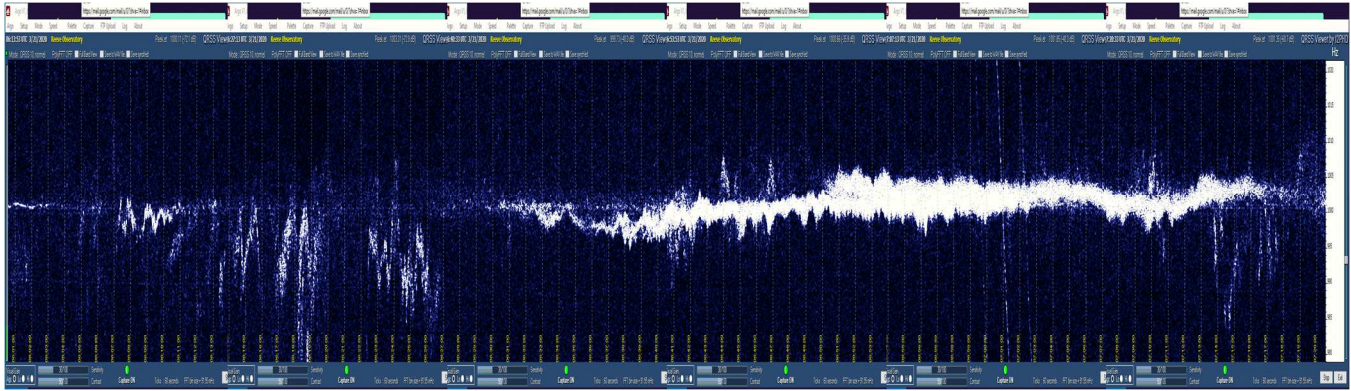


Figure 2.3.a ~ 21 March 2020 from 0601 to 0720 UTC. Composite of six spliced images corresponding to an 80-minute portion of the magnetogram below. Image stretched vertically to enhance the frequency shift. The beginning of the plot shows weak, discrete reflections with relatively large Doppler frequency shifts lasting about 20 minutes. These have a peak-peak frequency shift of about 20 Hz. The discrete reflections fade and are followed by steadier and stronger diffuse reflections with relatively low frequency drift. The diffuse trace is followed by additional discrete reflections that quickly fade. Reference: SS 0419 : SR 1552 UTC, LT=UTC-8

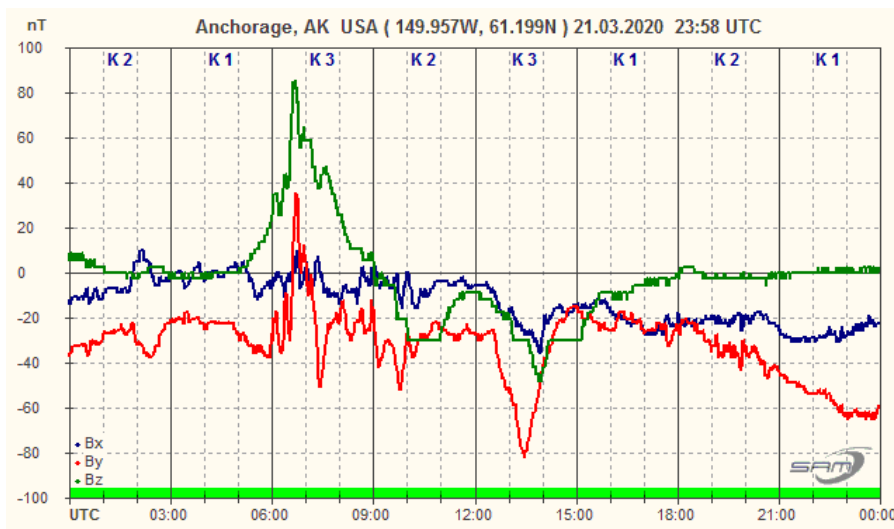


Figure 2-3.b ~ Magnetogram for the 24-hour period on 21 March 2020. The Argo plot above corresponds to the geomagnetic activity in By and Bz (red and green traces, respectively) starting near 0600 and lasting about 1 hour. Note the unrelated ultralow frequency (ULF) waves in By between 1530 and 2030.

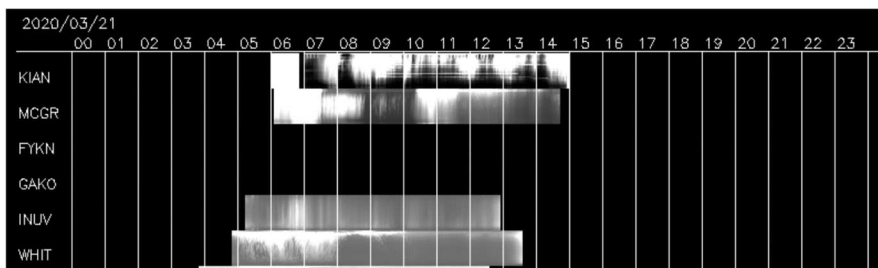


Figure 2-3.c ~ Keogram of all-sky images for 21 March 2020. All sites shown here indicate apparent aurora at the times of the above Argo plot.

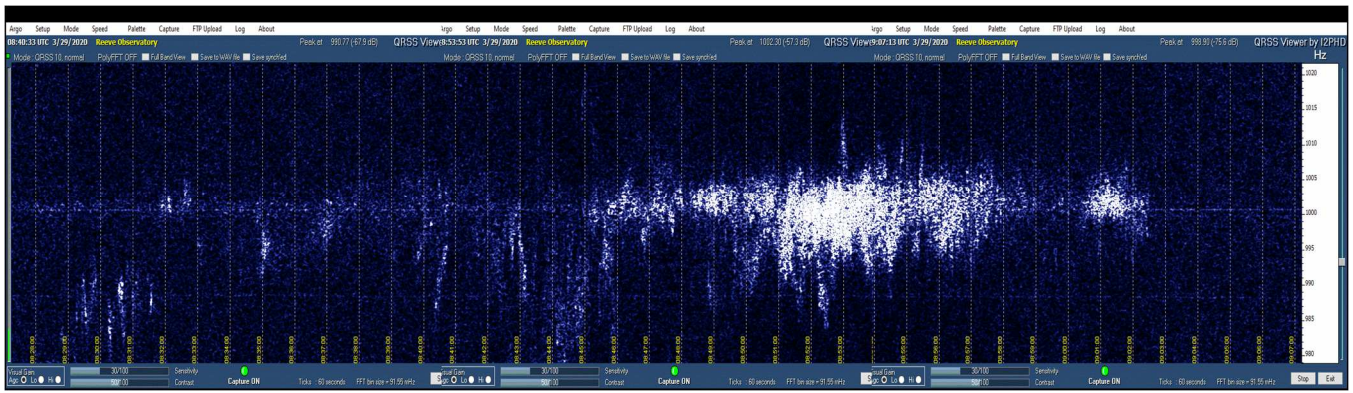


Figure 2-4.a ~ 29 March 2020 from 0828 to 0907 UTC. Composite of three images corresponding to a 39-minute portion of the magnetogram below. Image stretched vertically. The beginning of the plot shows weak, discrete reflections with relatively large Doppler frequency shifts lasting about 20 minutes. The Doppler shifted signals have a peak-peak frequency shift of about 20 Hz. These are followed by steadier and stronger diffuse reflections with relatively low frequency drift that fade after about 15 minutes. Reference: SS 0439 : SR 1526 UTC, LT=UTC-8

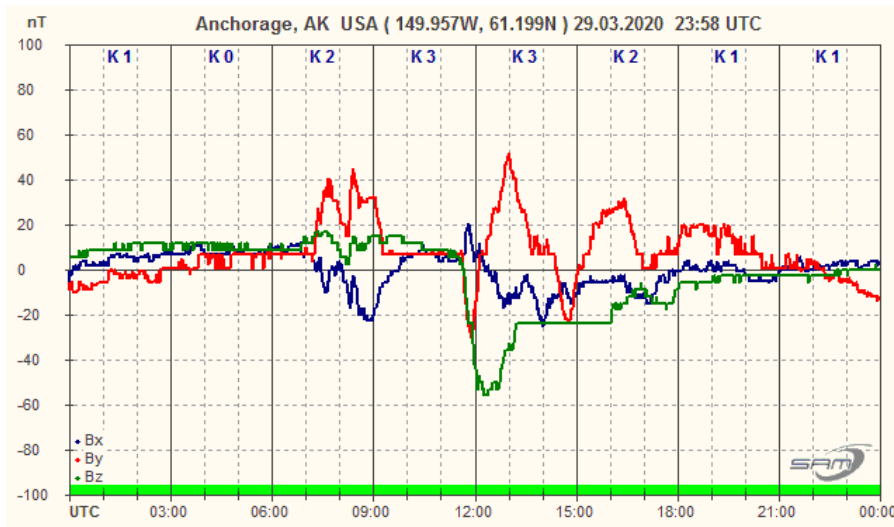


Figure 2-4.b ~ Magnetogram for the 24-hour period on 29 March 2020. The Argo plot above corresponds to the geomagnetic activity in Bx and By (blue and red traces, respectively) starting near 0700 and lasting about 2 hours.

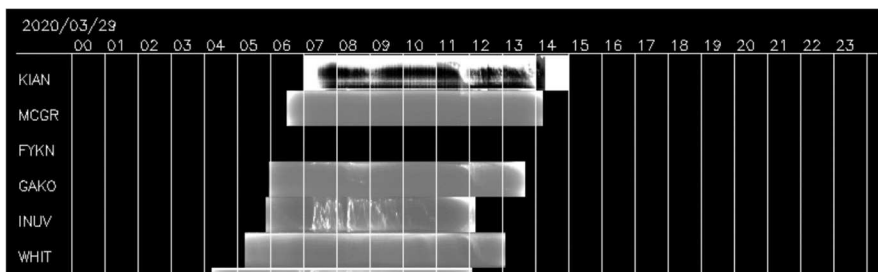


Figure 2-4.c ~ Keogram of all-sky images for 29 March 2020. The westward site KIAN and eastward site INUV show apparent aurora.

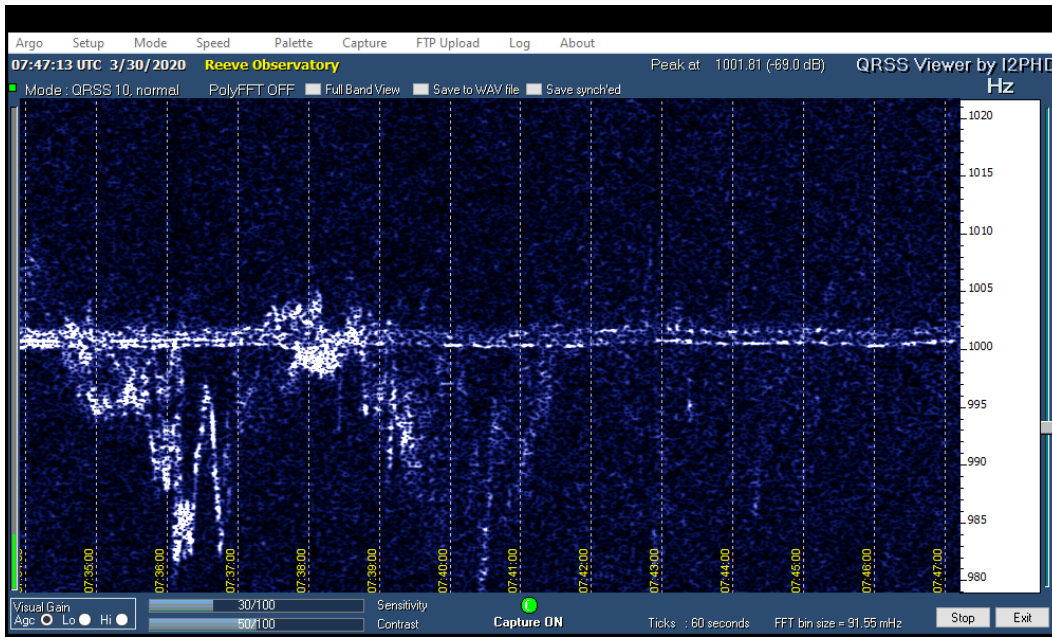


Figure 2-5.a ~ 30 March 2020 from 0734 to 0747 UTC. Single image corresponding to a 13-minute portion of the magnetogram below. The beginning of the plot appears to show both Doppler frequency shifted discrete reflections and steadier but very weak direct-path signals. The Doppler shifted reflections have a peak-peak frequency shift of at least 20 Hz, which is almost entirely negative. Reference: SS 0442 : SR 1523 UTC, LT=UTC-8

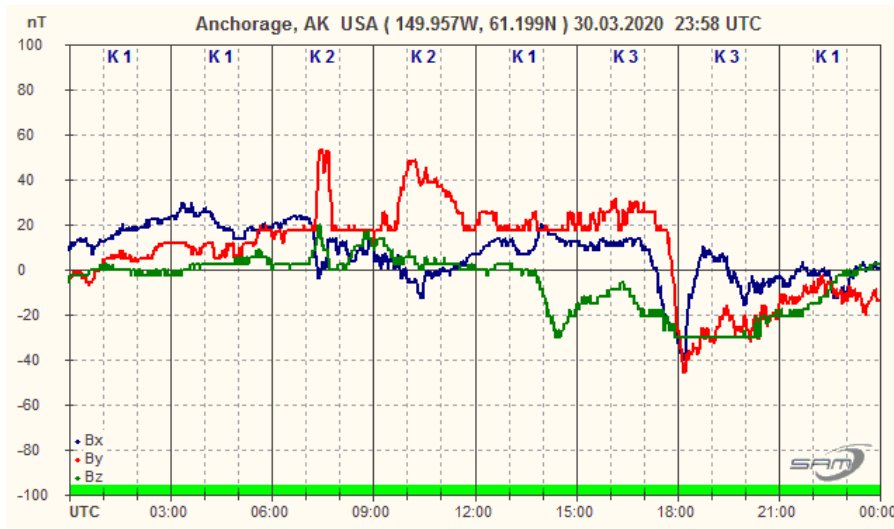


Figure 2-5.b ~ Magnetogram for the 24-hour period on 30 March 2020. The Argo plot above corresponds to the sharp geomagnetic activity in By (red trace) from approximately 0710 to 0750.

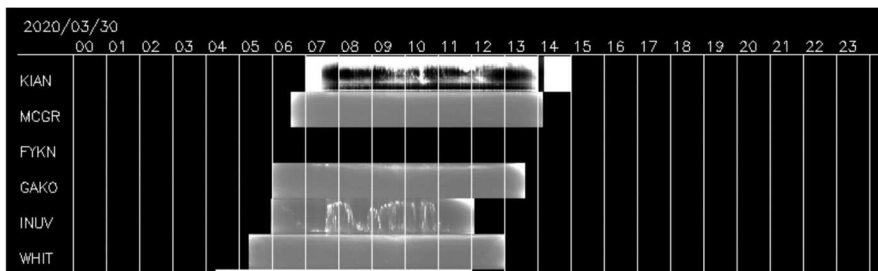


Figure 2-5.c ~ Keogram of all-sky images for 30 March 2020. KIAN and INUV show apparent aurora at the times of the above Argo plot.

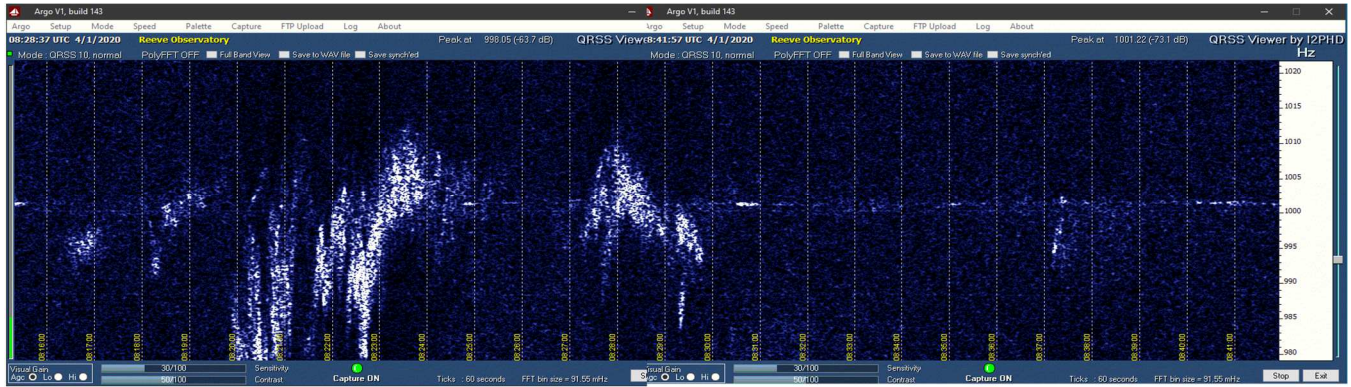


Figure 2-6.a ~ 1 April 2020 from 0816 to 0841 UTC. Composite of two images corresponding to a 26-minute portion of the magnetogram below. Image slightly stretched vertically. The reflections are entirely discrete type with peak-to-peak shift of 30 Hz and negative frequency bias. Reference: SS 0447 : SR 1520 UTC, LT=UTC-8

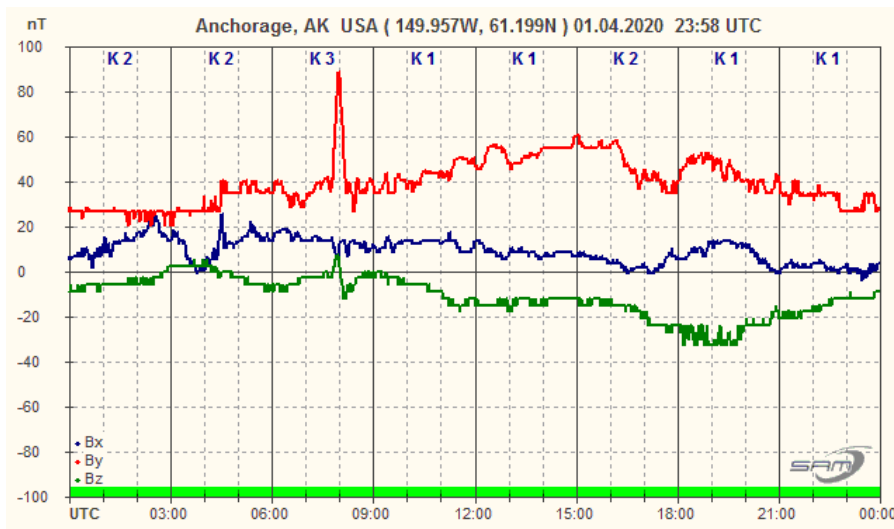


Figure 2-6.b ~ Magnetogram for the 24-hour period on 1 April 2020. The Argo plot above corresponds to the sharp geomagnetic activity in By (red trace) starting just before 0800.

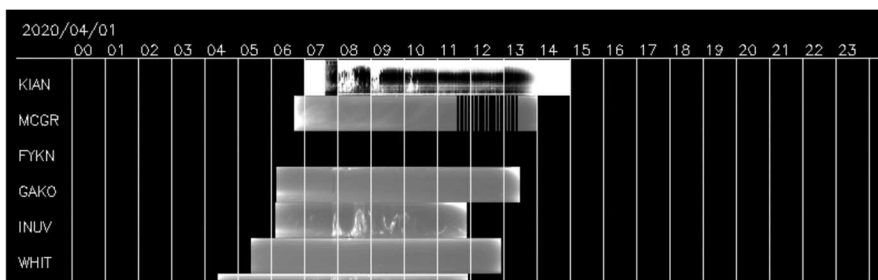


Figure 2-6.c ~ Keogram of all-sky images for 1 April 2020. Both KIAN and INUV show apparent aurora at the times of the above Argo plot.

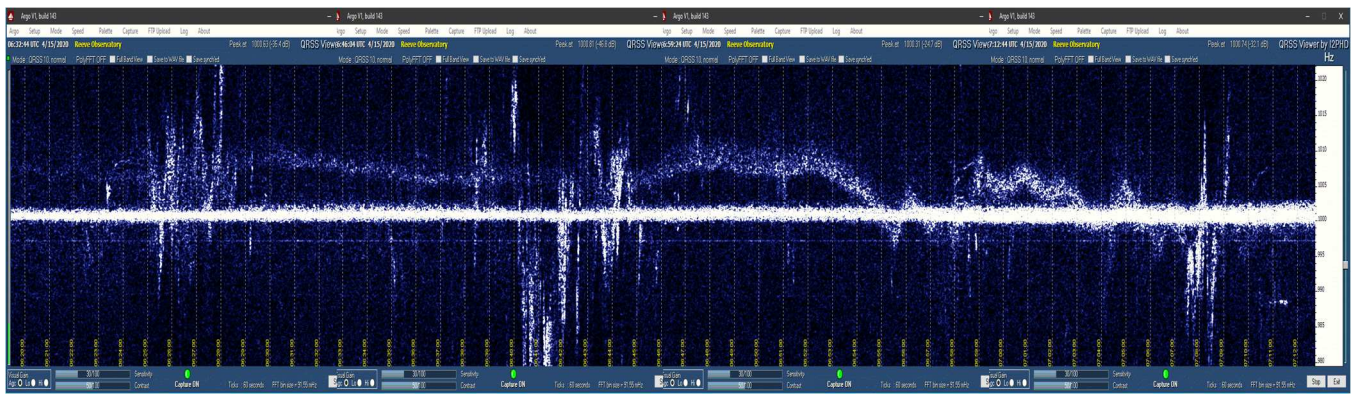


Figure 2-7.a ~ 15 April 2020 from 0620 to 0712 UTC. Composite of four images corresponding to a 52-minute portion of the magnetogram below. Image slightly stretched vertically. The beginning of the plot appears to show both Doppler frequency shifted reflections and steadier direct-path signals. The Doppler shifted signals have a peak-peak frequency shift of at least 40 Hz. A third signal also is apparent that is diffuse and slowly drifting with positive frequencies; this may be a spurious signal. Reference: SS 0523 : SR 1633 UTC, LT=UTC-8

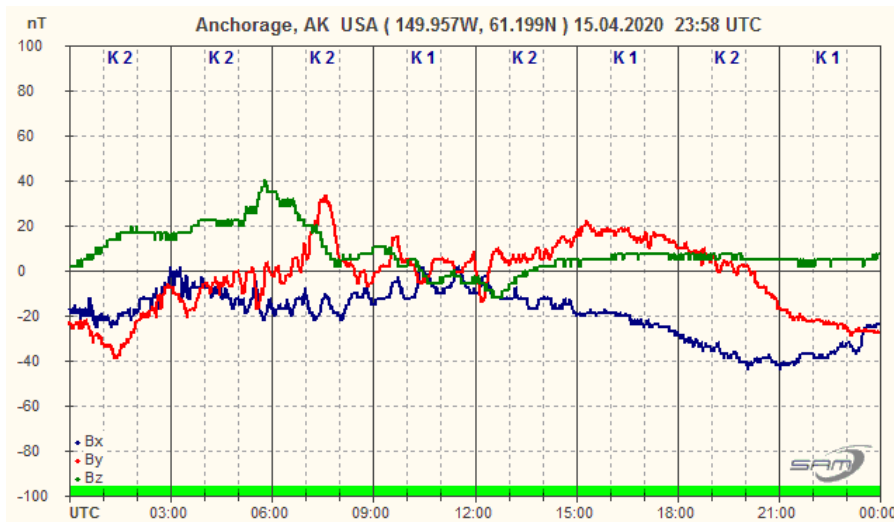


Figure 2-7.b ~ Magnetogram for the 24-hour period on 15 April 2020. The Argo plot above corresponds to the minor geomagnetic activity in By (red trace) from around 0630 to 0800.

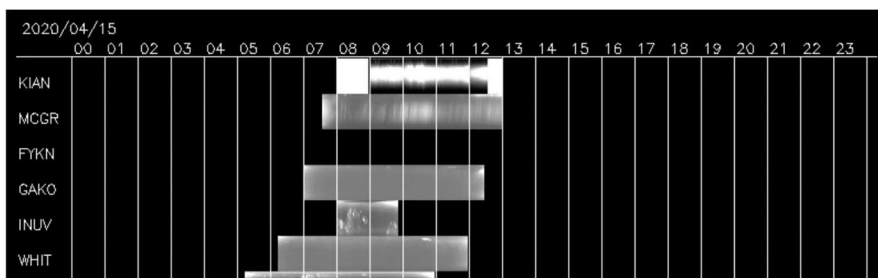


Figure 2-7.c ~ Keogram of all-sky images for 15 April 2020. No obvious aurora is seen at the times of the above Argo plot.

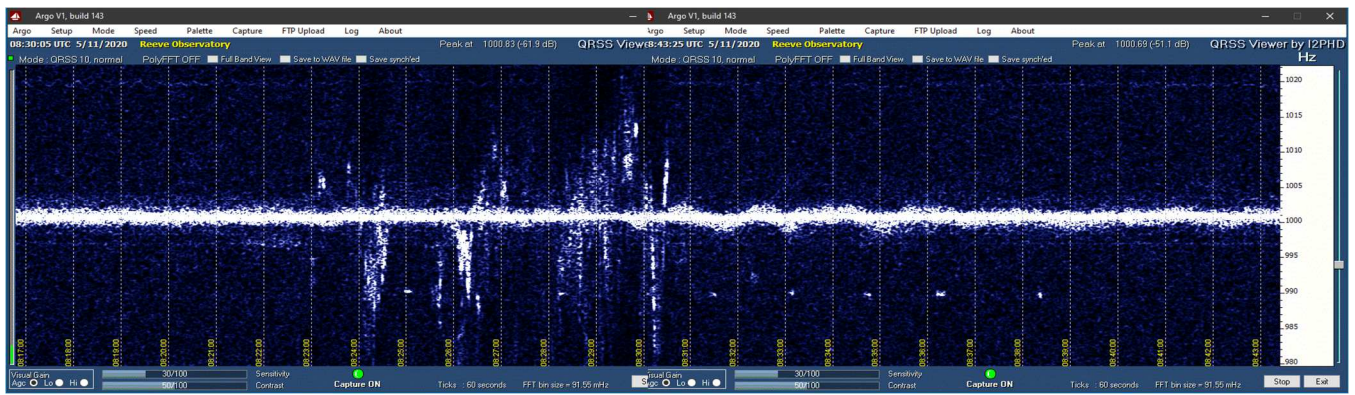


Figure 2-8.a ~ 11 May 2020 from 0817 to 0843 UTC. Composite of two images corresponding to a 26-minute portion of the magnetogram below. The plot appears to show both Doppler frequency shifted reflections and steadier direct-path signals, although the direct-path signals undergo some frequency deviation that begin when the signals with rapid frequency shift end. The Doppler shifted signals have a peak-peak frequency shift of -20 to $+12$ Hz. Short quasi-periodic spurious signals also are apparent that have a frequency of 990 Hz. Reference: SS 0632 : SR 1318 UTC, LT=UTC-8

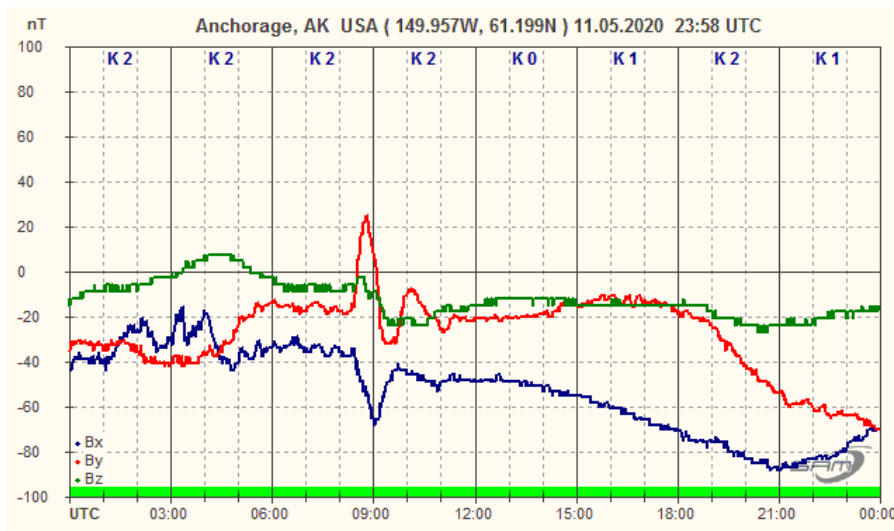


Figure 2-8.b ~ Magnetogram for the 24-hour period on 11 May 2020. The Argo plot above corresponds to the minor deflections in Bx and By (blue and red traces, respectively) from approximately 0820 to 0930 UTC.

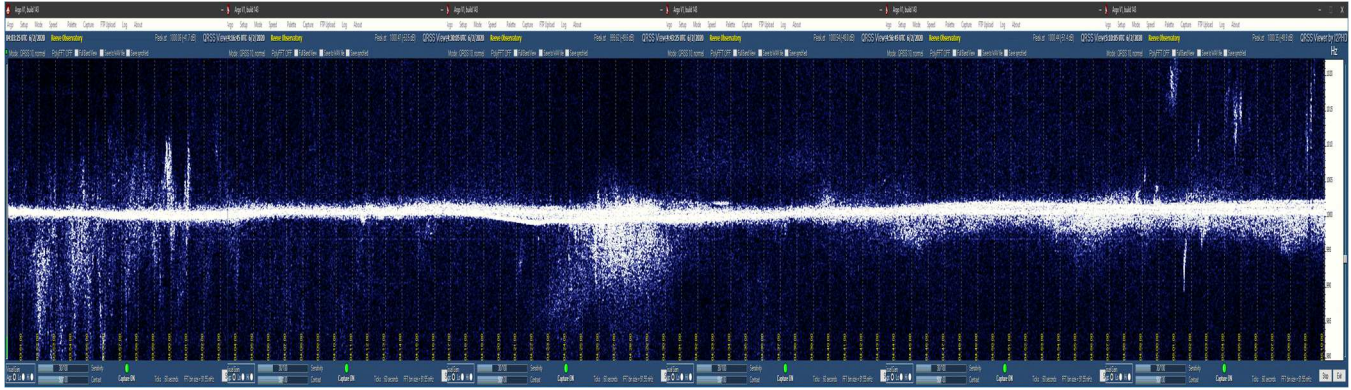


Figure 2-9.a ~ 2 June 2020 from 0351 to 0510 UTC. Composite of six images corresponding to a 79-minute portion of the magnetogram below. Image stretched vertically. The plot shows daytime aurora radio reflections and steadier direct-path signals, although the direct-path signals undergo small frequency deviations. The Doppler shifted reflections have a peak-peak frequency shift of -20 to $+20$ Hz and probably exceeded the 40 Hz displayed frequency span. Note the periodic structures starting as discrete reflections at the beginning, diffuse in the middle and discrete at the end. Reference: SS 0723 : SR 1232 UTC, LT=UTC-8

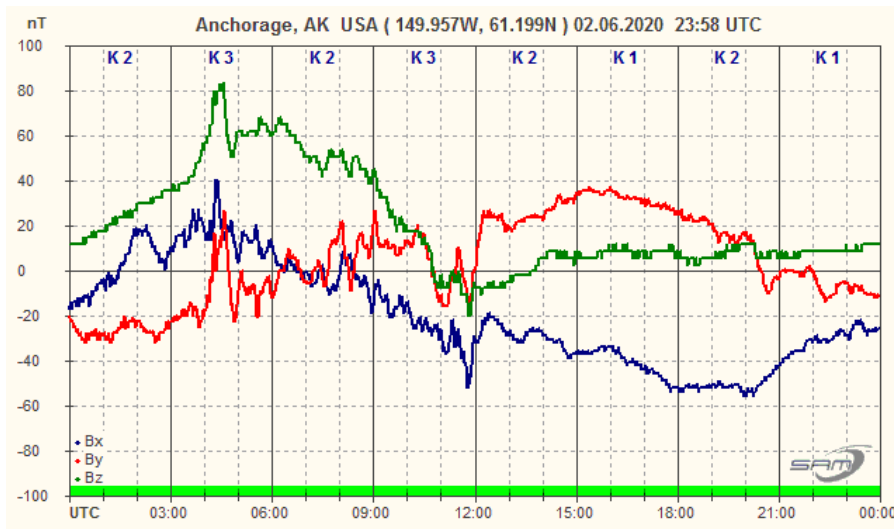


Figure 2-9.b ~ Magnetogram for the 24-hour period on 2 June 2020. The Argo plot above corresponds to the relatively minor deflections in all three magnetic components from approximately 0400 to 0510 UTC in all three magnetic components.

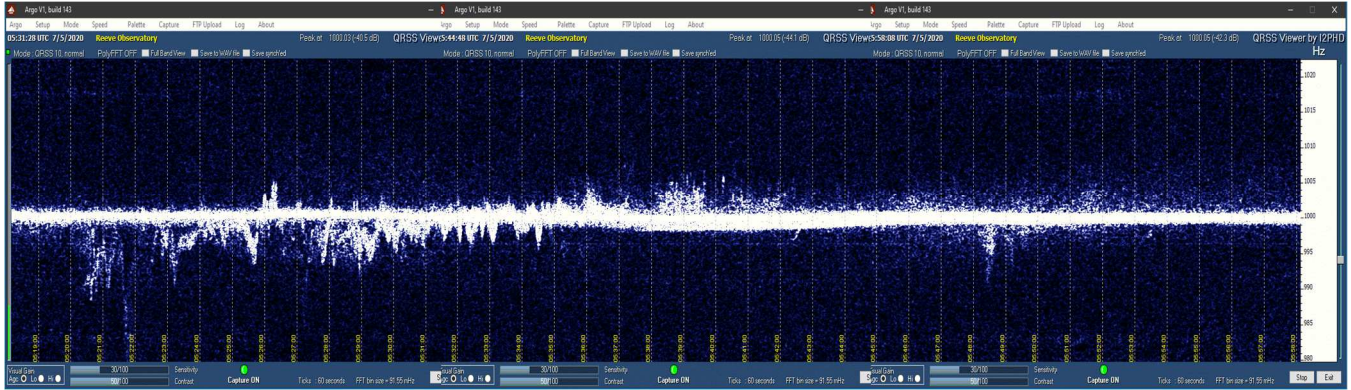


Figure 2-10.a ~ 5 July 2020 from 0519 to 0558 UTC. Composite of three images corresponding to a 39-minute portion of the magnetogram below. Image stretched vertically. This plot shows both daytime aurora radio reflections and steadier direct-path signals. The Doppler shifted signals have a peak-peak frequency shift of -17 to $+7$ Hz starting with negative shift and drifting to positive. Reference: SS 0733 : SR 1235 UTC, LT=UTC-8

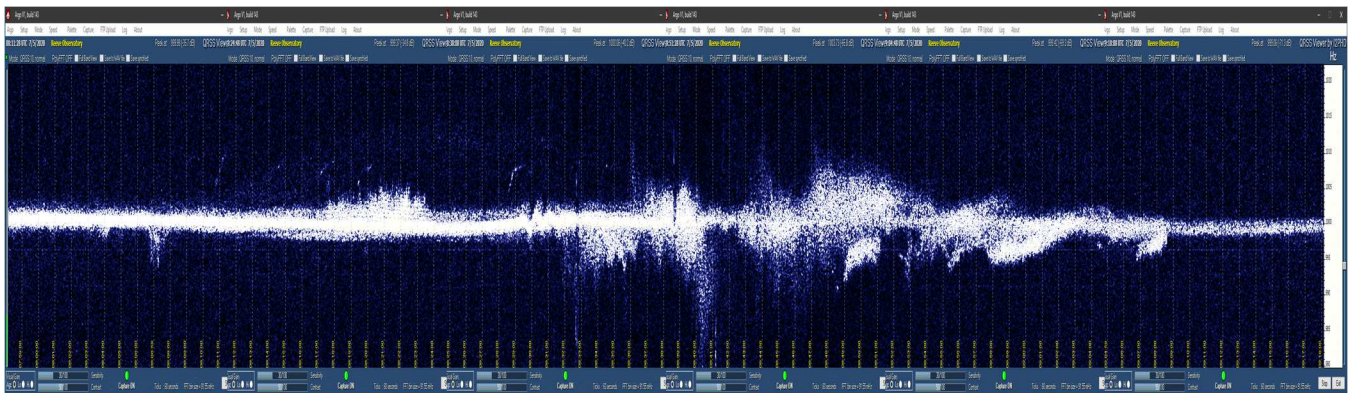


Figure 2-10.b ~ 5 July 2020 from 0759 to 0918 UTC, 2 hours after the previous plot. Composite of six images corresponding to a 78-minute portion of the magnetogram above. Image stretched vertically. The plot shows both aurora radio reflections and steadier direct-path signals soon after sunset. The Doppler shifted signals have a peak-peak frequency shift of -17 to $+10$ Hz. This and the previous Argo plot probably constitute a substorm. Reference: SS 0733 : SR 1235 UTC, LT=UTC-8

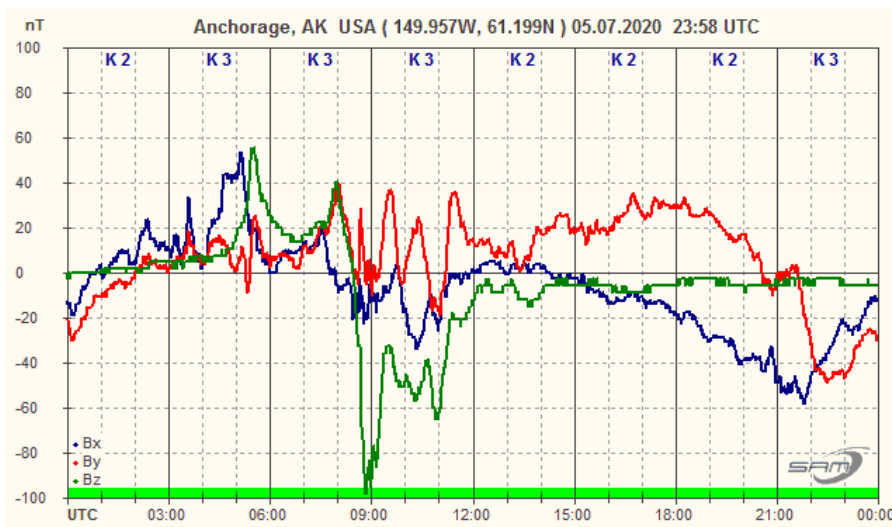


Figure 2-10.c ~ Magnetogram for the 24-hour period on 5 July 2020. The upper Argo plot corresponds to the relatively minor deflections in all three magnetic components from approximately 0520 to 0600 UTC. Additional rapid deflections in B_y and B_z from about 0800 to 0930 correspond to the lower Argo plot.



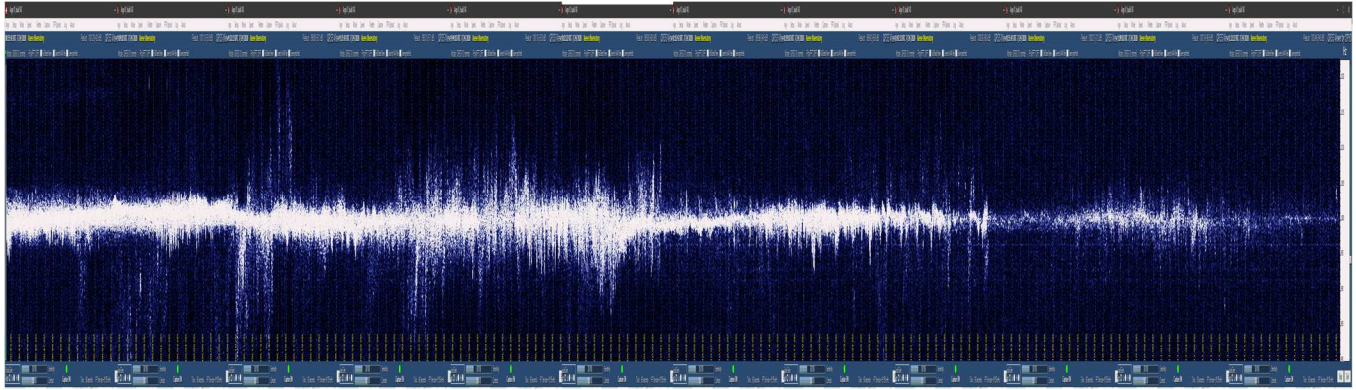


Figure 2-11.a ~ 24 July 2020 from 0843 to 1122 UTC. Composite of twelve images corresponding to a 2 h + 36 min portion of the magnetogram below. Image stretched vertically. The Doppler shifted signals have a peak-peak frequency shift of approximately -40 to $+30$ Hz, the amount of shift increasing and decreasing with a period of approximately 30 min. These traces appear to be a combination of discrete and diffuse reflections. Reference: SS 0656 : SR 1316 UTC, LT=UTC-8

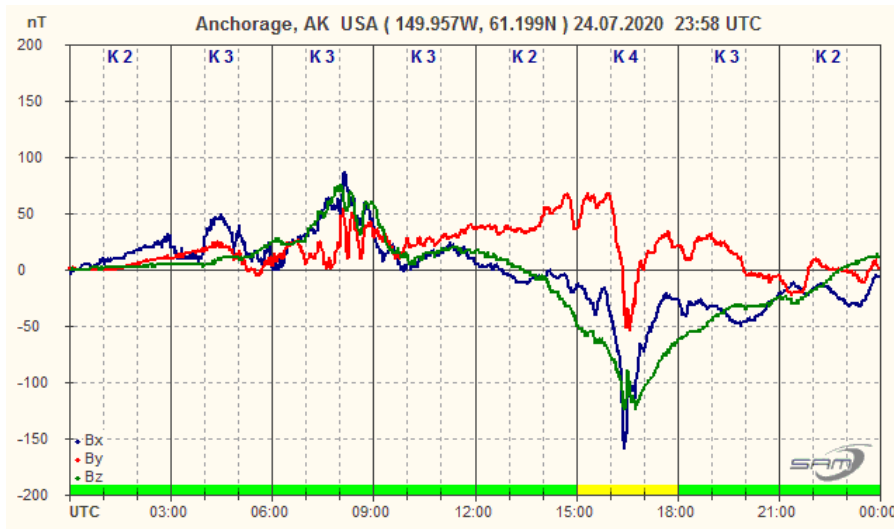


Figure 2-11.b ~ Magnetogram for the 24-hour period on 24 July 2020. The Argo plot above corresponds to the minor but sharp deflections from approximately 0800 to 1000 UTC in all three magnetic components. The deflections from about 1500 to 1730 led to additional Doppler frequency shifts but the corresponding Argo plots are not shown here.

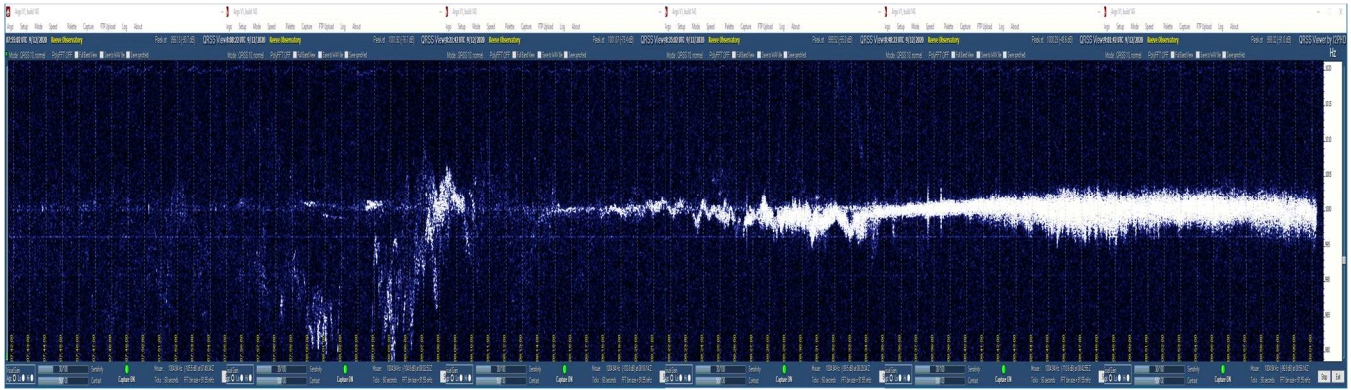


Figure 2-12.a ~ 12 September 2020 from 0741 to 0902 UTC. Composite of seven images corresponding to a 91 min portion of the magnetogram below. Image stretched vertically. The discrete reflections at the beginning have a peak-to-peak frequency shift of at least -40 Hz to $+10$ Hz. Note the reflections grow in intensity and then fade before changing to diffuse reflections. Also, note the abrupt loss of signal at the end of this plot, a behavior seen in other plots during 2020. Reference: SS 0428 : SR 1523 UTC, LT=UTC-8

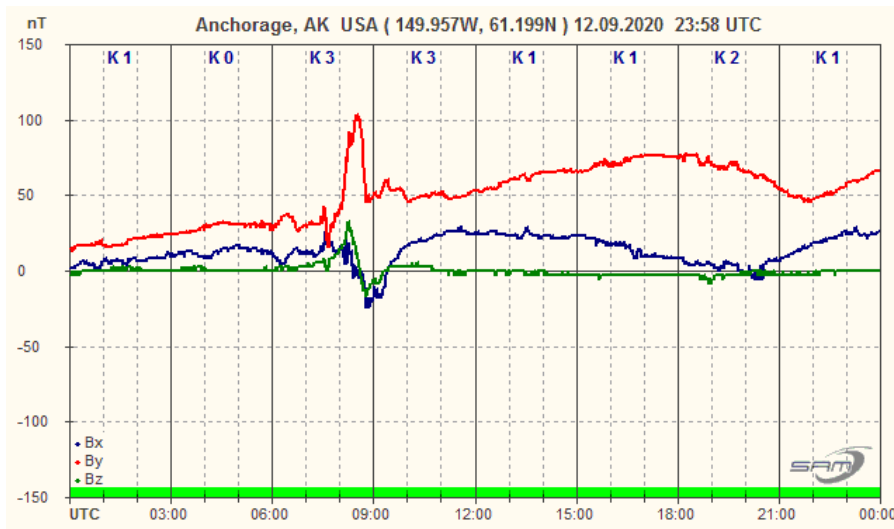


Figure 2-12.b ~ Magnetogram for the 24-hour period on 12 September 2020. The Argo plot above corresponds to the minor but rapid deflections in all three magnetic components starting about 0800 and progressing through 0900.

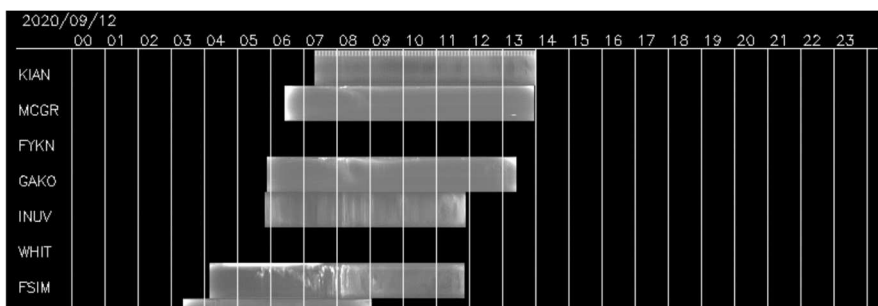


Figure 2-12.c ~ Keogram of all-sky images for 12 September 2020. Some aurora is apparent at FSIM at the times of the above Argo plot.

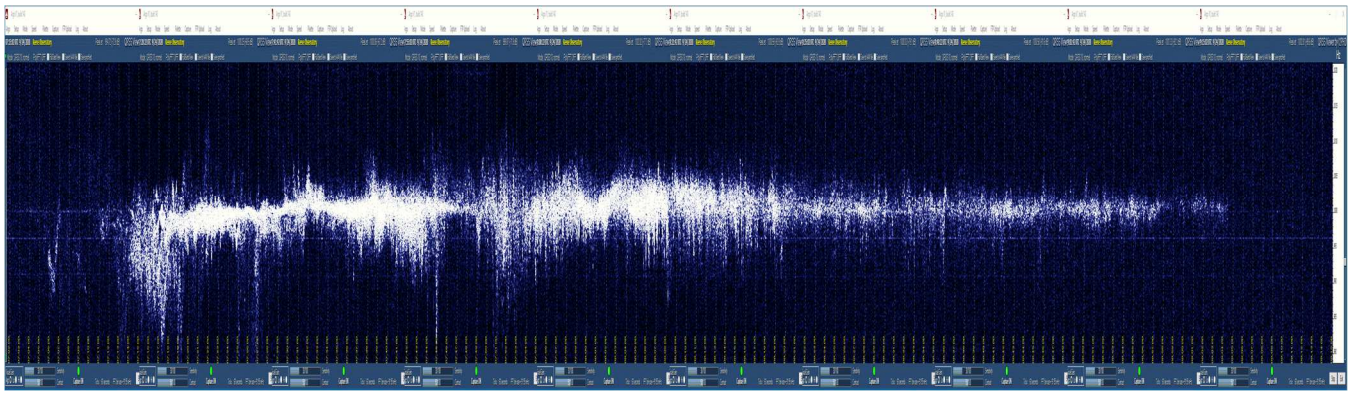


Figure 2-13.a ~ 24 September 2020 from 0702 to 0915 UTC. Composite of ten images corresponding to a 2-hour + 10 min portion of the magnetogram below. Image stretched vertically. The Doppler shifted signals have a peak-peak shift of at least -40 Hz to +10 Hz. Note the increases and decreases over time of the frequency shifts, most of which are diffuse in nature. The trace may represent a substorm. Reference: SS 0350 : SR 1552 UTC, LT=UTC-8

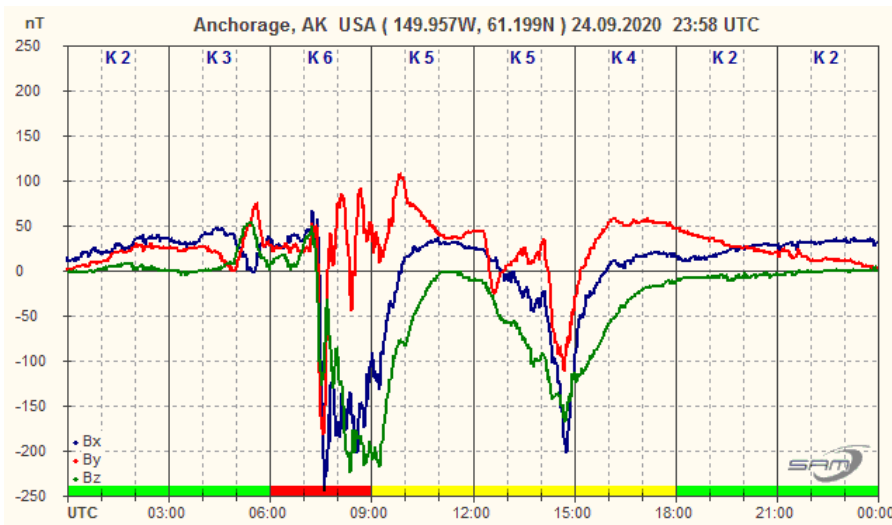


Figure 2-13.b ~ Magnetogram for the 24-hour period on 24 September 2020. The Argo plot above corresponds to the major and rapid deflections in all three magnetic components starting about 0700 and progressing through 1000. Additional deflections are observed in all three components between 1400 and 1500 but they did not produce any detectable aurora radio reflections.

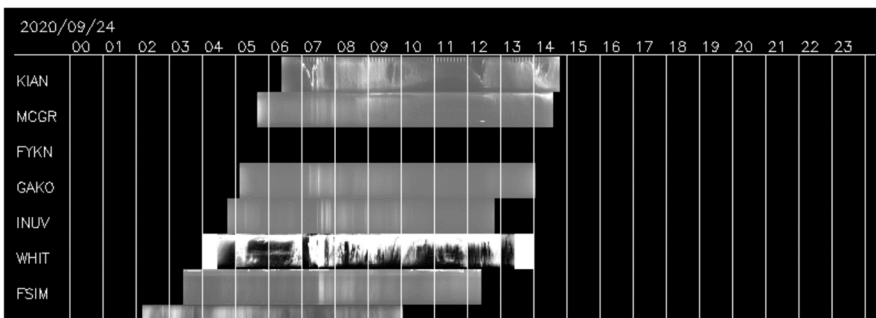


Figure 2-13.c ~ Keogram of all-sky images for 24 September 2020. Aurora is apparent at KIAN and WHIT at the times of the above Argo plot.

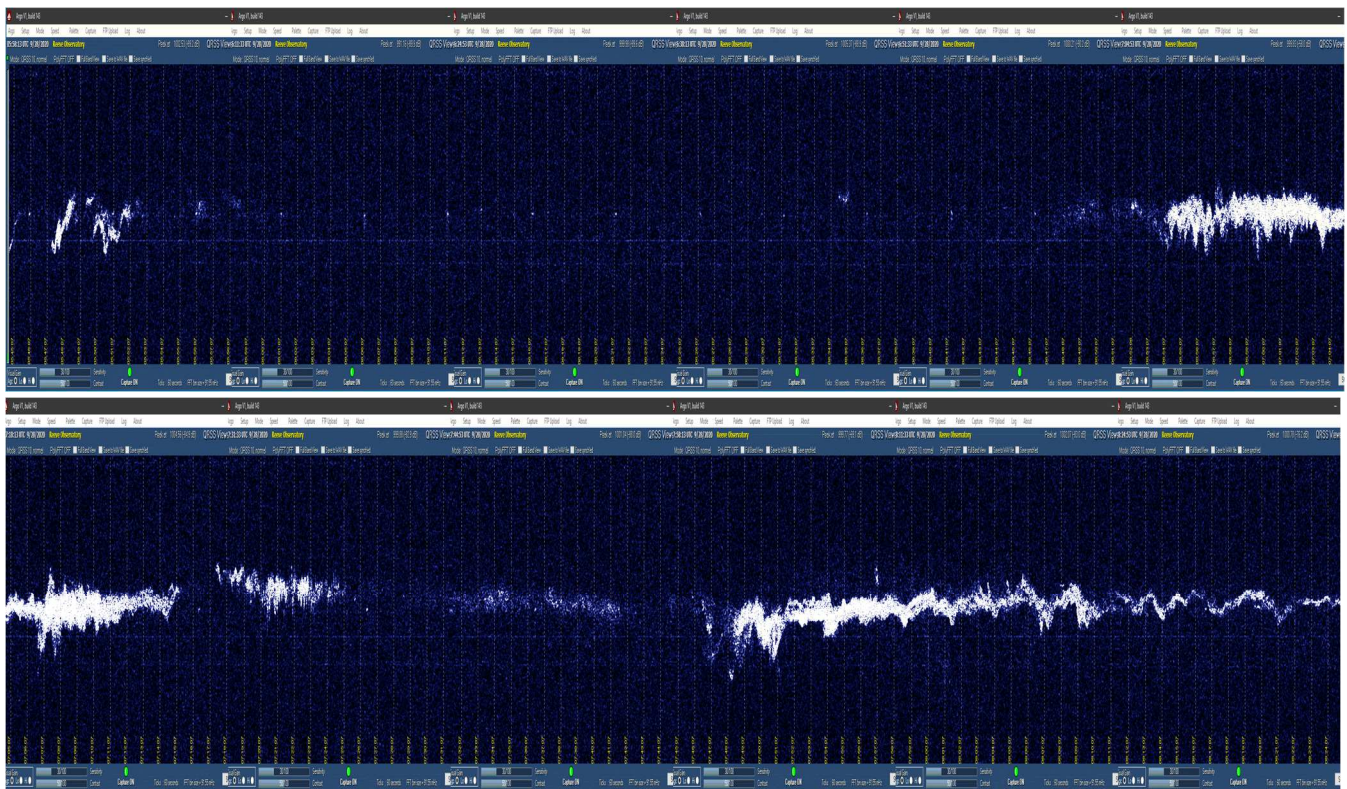


Figure 2-14.a ~ 28 September 2020 from 0545 to 0705 (upper plot) and 0705 to 0838 (lower plot). Each composite image consists of six individual images spliced together. Total elapsed time is 2 h + 36 min corresponding to the magnetogram below. Images stretched vertically. The series of images show a substorm. The upper image shows reflections lasting several minutes at the beginning followed by inactivity for about 1 h, at which time additional reflections are detected that continue into the lower image. There is another lull in the lower image followed by more reflections lasting approximately 40 min. The Doppler frequency shifts are modest, having a peak-to-peak range of about 10 Hz. Reference: SS 0338 : SR 1602 UTC, LT=UTC-8

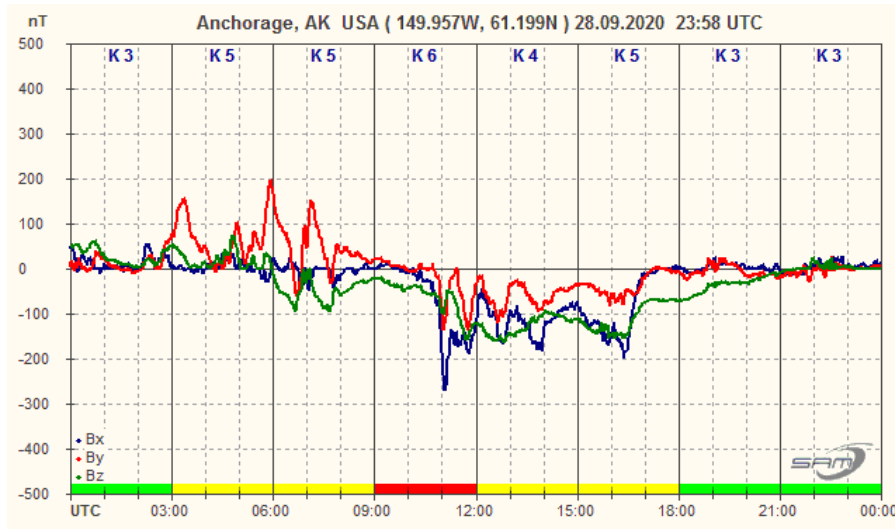


Figure 2-14.b ~ Magnetogram for the 24-hour period on 28 September 2020. The Argo plot above corresponds to the major and rapid deflections in all three magnetic components starting about 0530 and progressing through 0800. Additional deflections are observed in all three components between 1100 and 1700 but they did not produce any detectable aurora radio reflections.

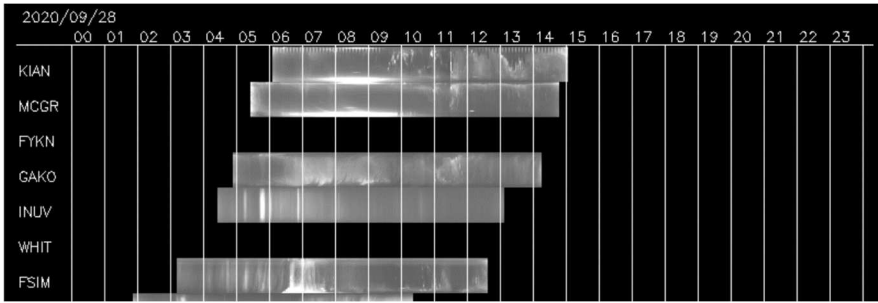


Figure 2-14.c ~ Keogram of all-sky images for 28 September 2020. Some weak aurora is visible at all sites during the times of the above Argo plot.

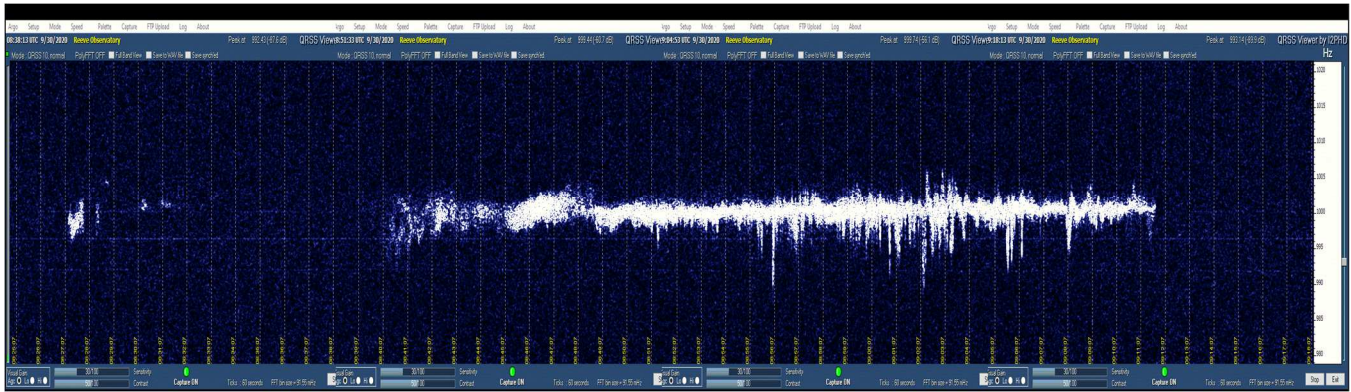


Figure 2-15.a ~ 30 September 2020 from 0825 to 0918. Composite of four images spliced together. The total elapsed time is 53 min corresponding to the magnetogram below. Image stretched vertically. Short but intense reflections are visible at the beginning of the plot. These quickly fade but return approximately 15 min later as diffuse reflections that morph into sharp, intense reflections. These continue for 30 min but abruptly end 6 min before the end of the plot. The Doppler frequency shifts are modest, having a peak-to-peak range of about 20 Hz. Reference: SS 0331 : SR 1607 UTC, LT=UTC-8

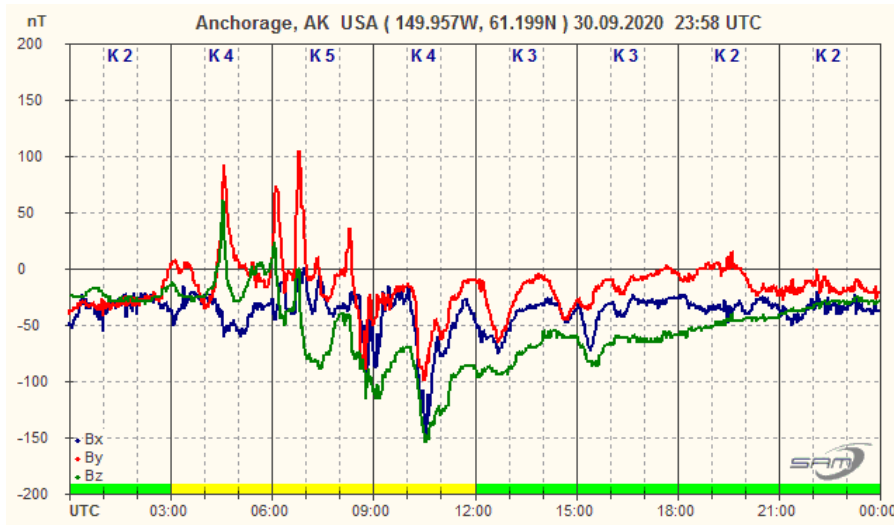


Figure 2-15.b ~ Magnetogram for the 24-hour period on 30 September 2020. The Argo plot above corresponds to the major and rapid deflections in all three magnetic components about 0900 and progressing through about 1000. The magnetic deflections prior to 0830 did not produce aurora radio reflections.

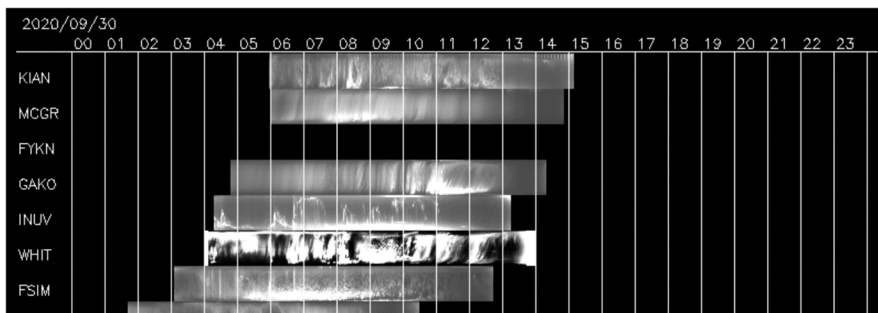


Figure 2-15.c ~ Keogram of all-sky images for 30 September 2020. All sites show varying amounts of aurora during the times of the above Argo plot.

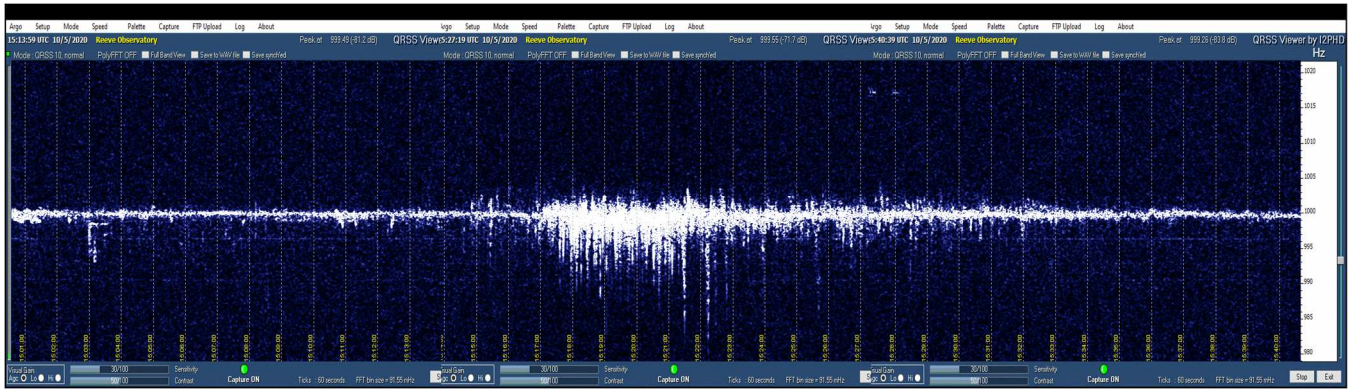


Figure 2-16.a ~ 5 October 2020 from 1501 to 1540. Composite image of three images spliced together. The total elapsed time is 39 min corresponding to the magnetogram below. Image slightly stretched vertically. This plot was made while the receivers were in the midnight-down sector. Aurora radio reflections are detected near the middle of the plot lasting about 15 min. The Doppler frequency shifts are moderate, having a peak-to-peak range of about 20 Hz. Reference: SS 0316 : SR 1620 UTC, LT=UTC-8

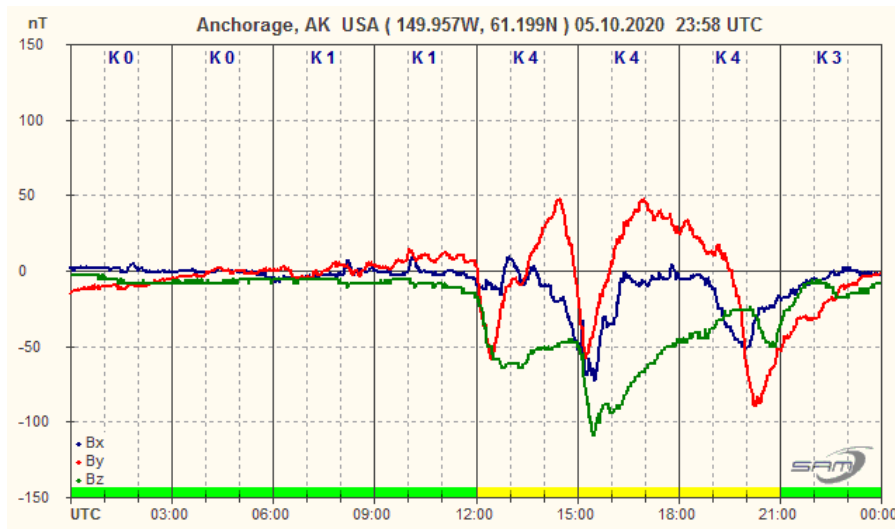


Figure 2-16.b ~ Magnetogram for the 24-hour period on 5 October 2020. The Argo plot above corresponds to the major and rapid deflections in all three magnetic components about 1430 and progressing through about 1530. The magnetic deflections before and after did not produce aurora radio reflections.

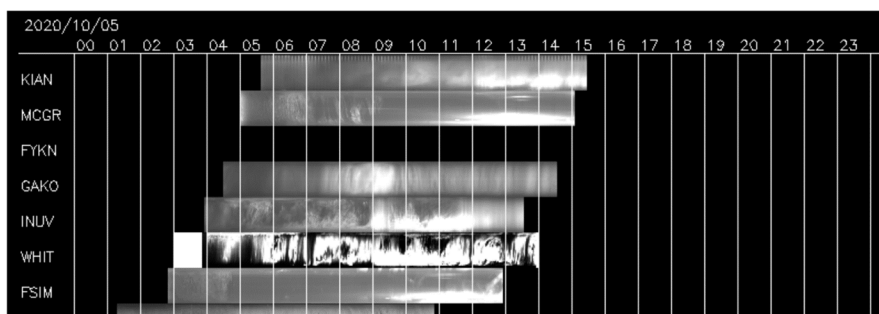


Figure 2-16.c ~ Keogram of all-sky images for 5 October 2020. Only the site KIAN was far enough west to record aurora at the times of the above Argo plot.

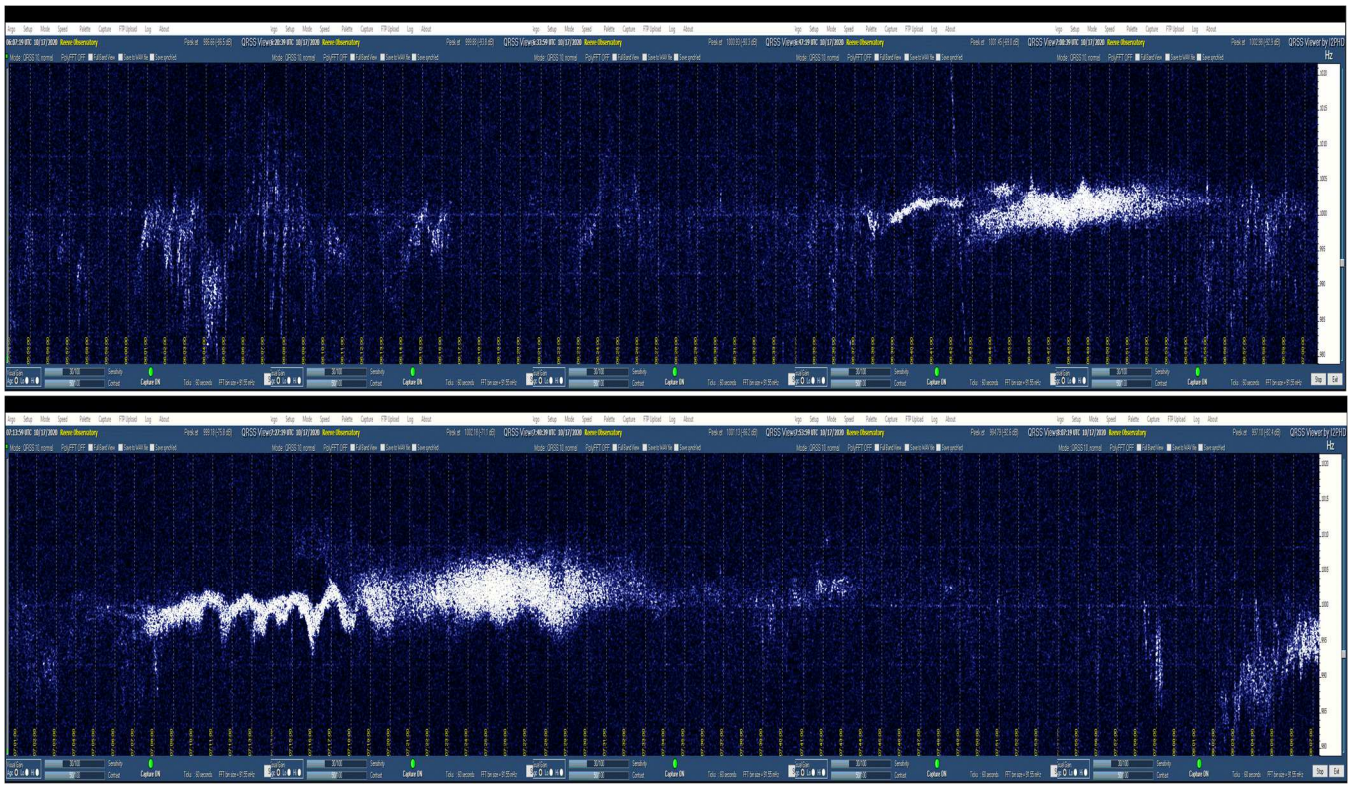


Figure 2-17.a ~ 17 October 2020 from 0554 to 0700 (upper plot) and 0700 to 0807 (lower plot). Composite images each consisting of five individual images spliced together. The total elapsed time is 2 h + 13 min corresponding to the magnetogram below. Images stretched vertically. The first two-thirds of the upper image show very weak discrete aurora radio reflections with an increase in intensity around 0638 that lasted approximately 30 min. The images together show the increases and decreases in intensity similar to the pattern seen in visible aurora reflections during a substorm. The Doppler frequency shifts reach a negative peak of -20 Hz while the positive peak is no more than $+10$ Hz. Reference: SS 0239 : SR 1604 UTC, LT=UTC-8

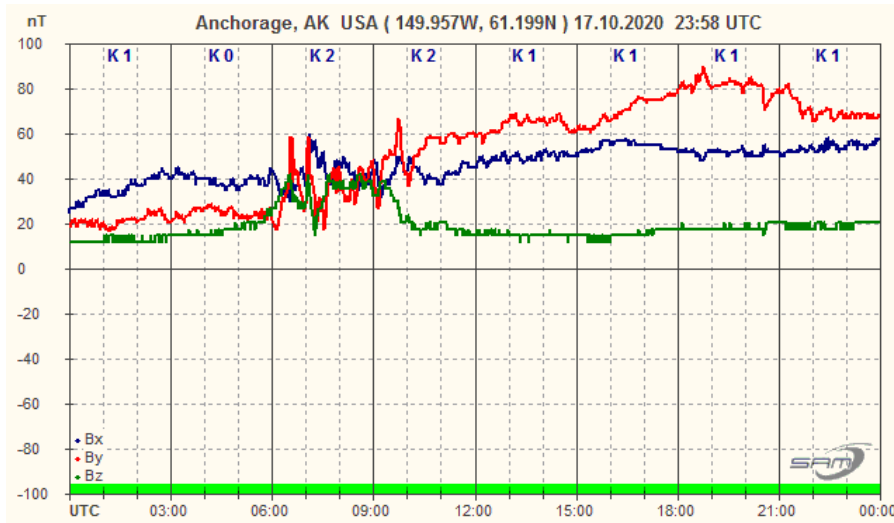


Figure 2-17.b ~ Magnetogram for the 24-hour period on 17 October 2020. The Argo plots above correspond to the rapid deflections in all three magnetic components between 0600 and 0900. Note that the magnetic variations during that time appear to be influenced by Ultra-Low Frequency (ULF) Waves.

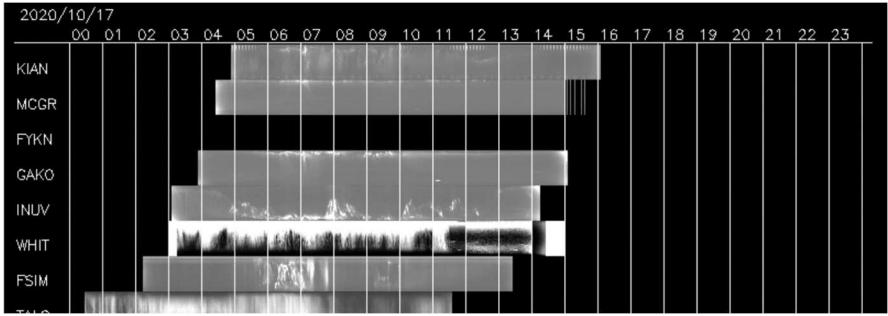


Figure 2-17.c ~ Keogram of all-sky images for 17 October 2020. Most sites indicate apparent aurora at the times of the above Argo plot, but the activity at the eastward sites WHIT and FSIM is the strongest.

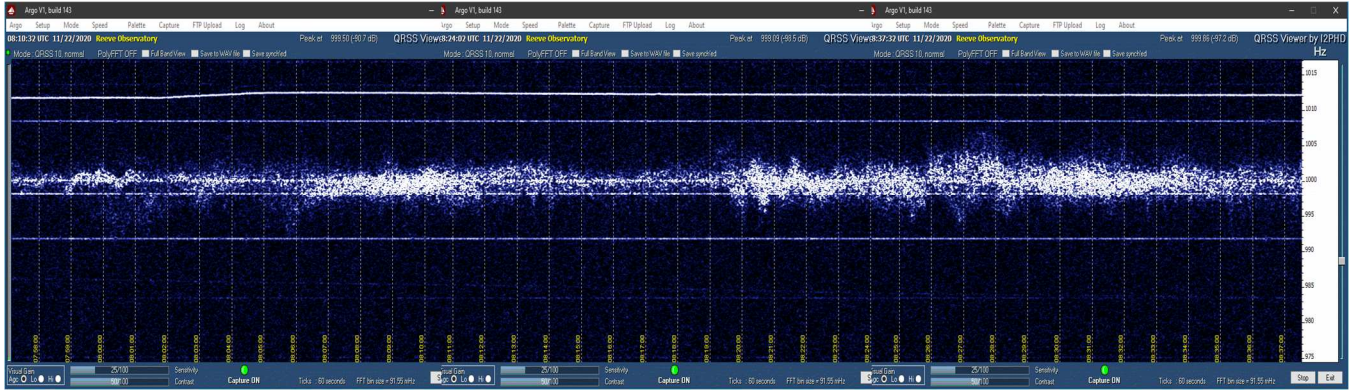


Figure 2-18.a ~ 22 November 2020 from 0759 to 0837 UTC. Composite of three images spliced together. Total elapsed time is 39 min corresponding to the magnetogram below. Image slightly stretched vertically. The reflections resulted in diffuse spectral features. The Doppler frequency shifts are modest, having a peak-to-peak range < 20 Hz. The thin horizontal lines are spurious signals. Reference: SS 0005 : SR 1651 UTC, LT=UTC-9

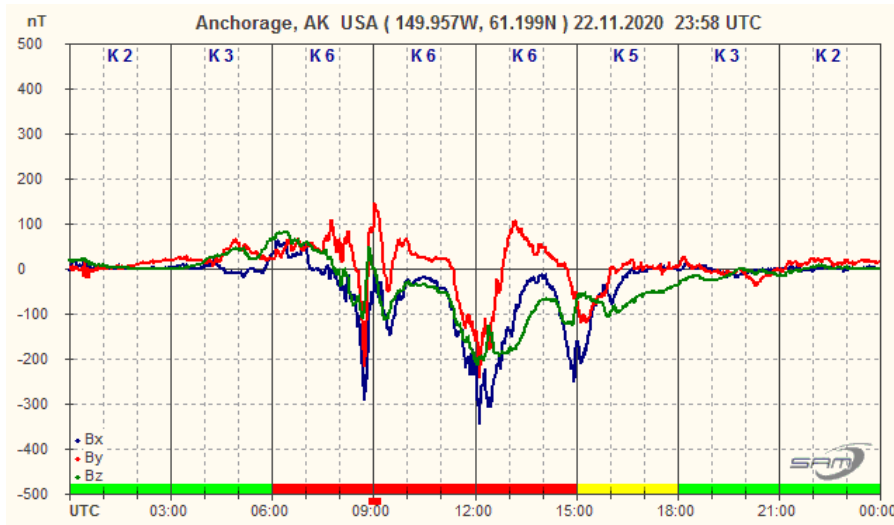


Figure 2-18.b ~ Magnetogram for the 24-hour period on 17 October 2020. The Argo plot above corresponds to the rapid deflections in all three magnetic components between 0800 and 0900. The deflections around 1200 and 1500 did not produce aurora radio reflections.

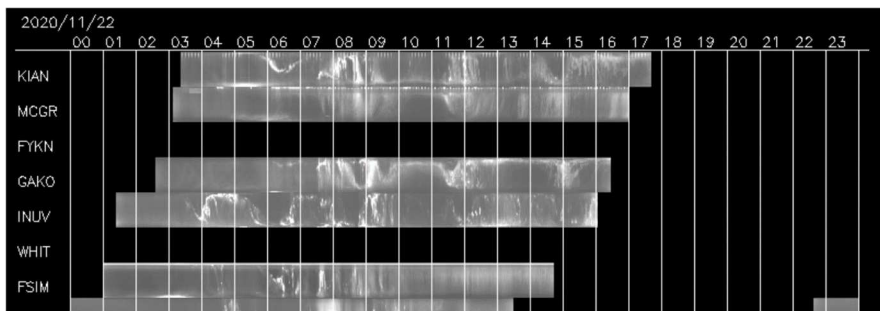


Figure 2-18.c ~ Keogram of all-sky images for 22 November 2020. All sites show apparent aurora at the times of the above Argo plot.

2-3. Discussion

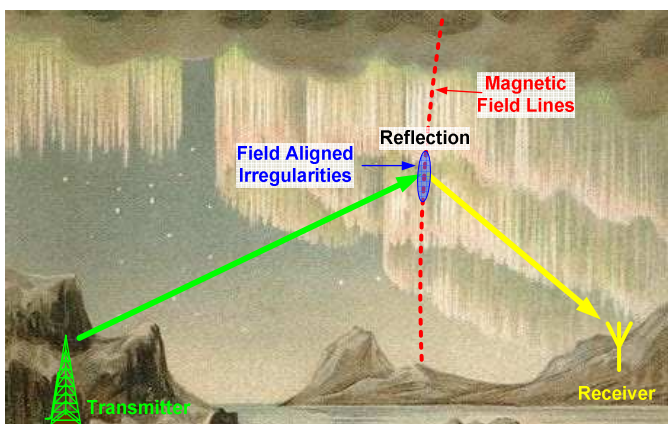
Transmissions from WWVH in Hawaii likely were the signal source for the aurora radio reflections received at Anchorage because of the favorable propagation geometry. It is thought that aurora radio reflections originated close to the northern horizon at low elevation angles (approximately 1° to 4°) with respect to Anchorage, corresponding to distances of 750 to 1000 km from the reflection region to Anchorage.

Occurrences of aurora radio detection at Anchorage depend on favorable HF propagation conditions from the transmitter to the aurora reflection region and back to the receiver. If these conditions did not exist, no detections were possible even though suitable reflection regions may have formed. There were many instances in 2020 with geomagnetic activity but no radio aurora was observed, which is attributed to lack of the required propagation geometry.

Most aurora radio reflections were detected before local solar midnight in the dusk-to midnight sector. A few were detected in the midnight to dawn sector, and a few were detected during daylight hours. It was noted in the 2020 observations that the gradient of the geomagnetic change was more important to detection of aurora radio than the amplitude of the change.

Both discrete and diffuse spectra were observed, but it is not known if these are related to different types of visible aurora or due to varying propagation effects or something else.

The 2020 observations were consistent with several aspects of the early investigations discussed in Part 1 including the high time correlation of aurora radio and geomagnetic activity, the radial speeds found through Doppler frequency calculations and the high fading rates. However, the Doppler frequency shifts seen in 2020 were biased toward negative values with most detections prior to local solar midnight. On the other hand, the early investigations indicated that detections prior to midnight had a positive shift. These apparently contrary results might be resolved through more investigations.



Source (with apologies):

<https://thegraphicsfairy.com/polar-lights-images/>



Author: Whitham Reeve obtained B.S. and M.S. degrees in Electrical Engineering at University of Alaska Fairbanks, USA. He worked as a professional engineer and engineering firm owner/operator in the airline and telecommunications industries for more than 40 years and now manufactures electronic equipment used in radio astronomy. He also is a part-time space weather advisor for the High-frequency Active Auroral Research Program (HAARP) and a member of the HAARP Advisory Committee. He has lived in Anchorage, Alaska his entire life. Email contact: whitreeve@gmail.com

Document Information

Author: Whitham D. Reeve

Copyright: © 2022 W. Reeve

Revisions: 0.0 (Original draft started, 21 Jan 2021)
0.1 (Work on introduction, 13 Feb 2021)
0.2 (Development of concepts, 28 Feb 2021)
0.3 (Revival, 15 Dec 2021)
0.4 (Added observations, 15-16 Feb 2022)
0.5 (Completed 1st draft, 25 Feb 2022)
0.6 (Add'l cleanup, 03 Mar 2022)
0.7 (Add'l cleanup, 11 Mar 2022)
0.8 (Final edits for distribution, 13 Mar 2022)
0.9 (Distribution, 05 Apr 2022)

Word count: 12719

File size (bytes): 29291706